

Wave Breaking Dissipation in a Young Wind Sea

MICHAEL SCHWENDEMAN AND JIM THOMSON

Applied Physics Laboratory, University of Washington, Seattle, Washington

JOHANNES R. GEMMRICH

Department of Physics and Astronomy, University of Victoria, Victoria, British Columbia, Canada

(Manuscript received 2 December 2012, in final form 1 October 2013)

ABSTRACT

Coupled in situ and remote sensing measurements of young, strongly forced wind waves are applied to assess the role of breaking in an evolving wave field. In situ measurements of turbulent energy dissipation from wave-following Surface Wave Instrument Float with Tracking (SWIFT) drifters and a tethered acoustic Doppler sonar system are consistent with wave evolution and wind input (as estimated using the radiative transfer equation). The Phillips breaking crest distribution $\Lambda(c)$ is calculated using stabilized shipboard video recordings and the Fourier-based method of Thomson and Jessup, with minor modifications. The resulting $\Lambda(c)$ are unimodal distributions centered around half of the phase speed of the dominant waves, consistent with several recent studies. Breaking rates from $\Lambda(c)$ increase with slope, similar to in situ dissipation. However, comparison of the breaking rate estimates from the shipboard video recordings with the SWIFT video recordings show that the breaking rate is likely underestimated in the shipboard video when wave conditions are calmer and breaking crests are small. The breaking strength parameter b is calculated by comparison of the fifth moment of $\Lambda(c)$ with the measured dissipation rates. Neglecting recordings with inconsistent breaking rates, the resulting b data do not display any clear trends and are in the range of other reported values. The $\Lambda(c)$ distributions are compared with the Phillips equilibrium range prediction and previous laboratory and field studies, leading to the identification of several inconsistencies.

1. Introduction

Wave breaking plays a primary role in the surface wave energy balance. The evolution of a wave energy spectrum in frequency $E(f)$ is governed by the radiative transfer equation (RTE):

$$\frac{\partial E(f)}{\partial t} + (\mathbf{c}_g \cdot \nabla) E(f) = S_{in}(f) + S_{nl}(f) - S_{ds}(f), \quad (1)$$

where $S_{in}(f)$, $S_{nl}(f)$, and $S_{ds}(f)$ are the source terms corresponding to wind input, nonlinear interactions, and dissipation, respectively, and \mathbf{c}_g is the wave group velocity, assuming minimal surface currents (Young 1999). Wave breaking is thought to be the dominant mechanism for energy dissipation (Gemmrich et al. 1994; Babanin et al. 2010b), though recent evidence suggests

that nonbreaking “swell” dissipation may be significant when breaking is not present (Babanin and Haus 2009; Rogers et al. 2012; Babanin and Chalikov 2012). Dissipation by breaking is widely considered to be the least well-understood term and process in wave mechanics (Banner and Peregrine 1993; Thorpe 1995; Melville 1996; Duncan 2001; Babanin 2011). In particular, there have been only a few field studies that quantify the wave energy lost to whitecaps in deep water.

Much of the energy lost during wave breaking is dissipated as turbulence in the ocean surface layer. Several studies (Kitaigorodskii et al. 1983; Agrawal et al. 1992; Anis and Moum 1995; Terray et al. 1996) have shown a layer of enhanced dissipation under breaking waves. Below this enhanced layer, measurements tend to approach the expected “law of the wall” scaling associated with flow over a solid, flat boundary. Gemmrich and Farmer (2004) correlated enhanced dissipation with breaking events, suggesting that dissipation in this surface layer corresponds to energy lost from breaking waves. Thus, measurements of turbulent dissipation can

Corresponding author address: Michael Schwendeman, University of Washington, 1013 NE 40th Street, Box 355640, Seattle, WA 98105-6698.

E-mail: mss28@u.washington.edu

be used as a proxy estimate of breaking dissipation. However, these are lower bound estimates, as some wave energy is also spent on work done in the submersion of bubbles [as much as 50% according to Loewen and Melville (1991)].

Gemmrich (2010) measured turbulent dissipation in the field using a system of three high-resolution pulse-coherent SonTek DopBeam acoustic Doppler sonars, profiling upward into the wave crest above the mean water line. Gemmrich (2010) found that turbulence was enhanced particularly in the crest, even more so than previous observations. Thomson (2012) achieved a similar result with wave-following Surface Wave Instrument Float with Tracking (SWIFT) drifters, which measure turbulent dissipation from near the surface to a 0.5-m depth with a pulse-coherent Nortek Aquadopp HR acoustic Doppler profiler. Both of these studies estimate dissipation rate using the second-order structure function $D(z, r)$, as described in section 2 and in Wiles et al. (2006).

Using laboratory measurements, Duncan (1981, 1983) related the speed of a steady breaking wave to its energy dissipation rate. Towing a hydrofoil through a long channel at a constant speed and depth, Duncan (1981) determined that the rate of energy loss followed the scaling

$$\epsilon_l \propto \frac{\rho_w c^5}{g}, \quad (2)$$

where ϵ_l is the energy dissipation per crest length, ρ_w is the water density, g is gravitational acceleration, and c is the speed of the towed hydrofoil. Melville (1994) examined data from previous laboratory experiments of unsteady breaking (Loewen and Melville 1991) and noted an additional dependence of dissipation on wave slope, as also suggested in Duncan (1981). Drazen et al. (2008) used a scaling argument and a simple model of a plunging breaker to hypothesize that dissipation depends on wave slope to the $5/2$ power. They compiled previous data and made additional laboratory measurements and found roughly the expected dependence on slope.

In parallel with Duncan's work, Phillips (1985) introduced a statistical description of breaking $\Lambda(c, \theta)$, which is defined as the distribution of breaking crest lengths per area as a function of speed c and direction θ . Thus, the total length of breaking crests per area is

$$L_{\text{total}} = \int_0^\infty \int_0^{2\pi} \Lambda(c, \theta) c d\theta dc. \quad (3)$$

The scalar distribution $\Lambda(c)$ is often used in place of the full directional distribution. It can be found by integrating over all directions in broadband waves or by using the speed in the dominant direction in sufficiently

narrowbanded wave fields. The breaking rate, or breaker passage rate, is the frequency that an actively breaking crest will pass a fixed point in space. The breaking rate can be calculated from the first moment of $\Lambda(c)$:

$$R_\Lambda = \int c \Lambda(c) dc. \quad (4)$$

Phillips (1985) used Duncan's scaling to propose a relation for the total breaking-induced dissipation from the $\Lambda(c)$ distribution:

$$S_{\text{ds}, \Lambda} = \int \epsilon(c) dc = \frac{b \rho_w}{g} \int c^5 \Lambda(c) dc, \quad (5)$$

where b is a "breaking strength" proportionality factor, and $\epsilon(c)$ is the spectral dissipation function in phase speed.

In addition, Phillips (1985) hypothesized that at wavenumbers sufficiently larger than the peak, a spectral equilibrium range exists such that wind input, nonlinear transfers, and dissipation are all of the same order and spectral shape. Phillips (1985) proposed a spectral form of the dissipation function within the equilibrium range:

$$\epsilon(c) = 4\gamma\beta^3 I(3p) \rho_w u_*^3 c^{-1}, \quad (6)$$

where

$$I(3p) = \int_{-\pi/2}^{\pi/2} (\cos\theta)^{3p} d\theta \quad (7)$$

is a directional weight function; γ , β , and p are constants; and u_* is the wind friction velocity. Thus, Phillips derived that, within the equilibrium range, $\Lambda(c)$ should follow c^{-6} and be given by

$$\Lambda(c) = (4\gamma\beta^3) I(3p) b^{-1} u_*^3 g c^{-6}. \quad (8)$$

The $\Lambda(c)$ formulation is well suited to remote sensing methods, which have shown promise in the field because of their ability to capture more breaking events than in situ point measurements. Early remote studies such as Ding and Farmer (1994) and Gemmrich and Farmer (1999) calculated wave breaking statistics without using $\Lambda(c)$. Later, the Duncan–Phillips formulation was recognized as a potential means to relate remote-sensed whitecap measurements to dissipation. Phillips et al. (2001) produced the first field observations of $\Lambda(c)$ using backscatter from radar data. Melville and Matusov (2002) used digital video taken from an airplane to calculate $\Lambda(c)$. Gemmrich et al. (2008) also calculated $\Lambda(c)$ from digital video, in this case from the Research Vessel

(R/V) *Floating Instrument Platform (FLIP)*. The studies of Kleiss and Melville (2010), Kleiss and Melville (2011), and Romero et al. (2012) all used $\Lambda(c)$ measurements from airplane video during the Gulf of Tehuantepec Experiment (GOTEX).

The results of Thomson and Jessup (2009) and Thomson et al. (2009) are of particular relevance to the present work. Thomson and Jessup (2009) introduced a Fourier-based method for processing shipboard video data into $\Lambda(c)$ distributions. The Fourier method has the advantage of increased efficiency and robust statistics compared to conventional time-domain crest-tracking methods. This method was validated alongside an algorithm similar to the one used in Gemmrich et al. (2008). Thomson et al. (2009) presented the results of the Fourier method for breaking waves in Lake Washington and Puget Sound in Washington State.

Despite the widely varying wave conditions, experimental methods, and processing techniques, a number of similar characteristics can be seen in the $\Lambda(c)$ results from these recent studies. With the exception of Melville and Matusov (2002), all of the $\Lambda(c)$ show a unimodal distribution with a peak at speeds roughly half the dominant phase speed. Melville and Matusov (2002) instead calculated a monotonically decreasing $\Lambda(c)$, but had limited resolution and used an assumption that the rear of the breaking crests was stationary. Kleiss and Melville (2011) demonstrated that the rear of a whitecap is not in fact stationary, and the differing result from Melville and Matusov (2002) could be reproduced in their data by imitating the study's video processing method. The peaked distribution differs from the c^{-6} shape predicted by Phillips (1985), though most studies note tails in $\Lambda(c)$ approaching c^{-6} at high speeds. These speeds, however, are not generally within the equilibrium range used to arrive at Eq. (8). Plant (2012) recently suggested that the unimodal $\Lambda(c)$ distributions are produced by an interference pattern of dominant wind waves, moving at speeds slightly less than the group velocity and resulting in large wave slopes during constructive interference. Another similarity in recent $\Lambda(c)$ studies is the dominance of infrequent, fast-moving whitecaps in the distribution of the fifth-moment $c^5\Lambda(c)$, which is used to calculate dissipation. Plots of $c^5\Lambda(c)$ often show significant values up to the highest speed bin for which they are calculated.

Knowledge of b is crucial to the remote calculation of dissipation. Values of b from the field have spanned four orders of magnitude, from 3.2×10^{-5} in Gemmrich et al. (2008) to 1.7×10^{-2} in Thomson et al. (2009). One issue appears to be the different choices made in processing $\Lambda(c)$, in particular defining the whitecap speed and length. Kleiss and Melville (2011) reviewed the methods

of Gemmrich et al. (2008) and Kleiss and Melville (2010) and noted a 300% difference in b resulting from their differing speed and length definitions.

Another problem is uncertainty over the nature of b . In introducing the concept, Phillips (1985) treated b as a constant; however, as noted above, the studies of Melville (1994) and Drazen et al. (2008) indicate at least one secondary dependence on wave slope. Wave slope can be represented in a number of ways from the wave spectrum $E(f)$. In Banner et al. (2000), the breaking probability of dominant waves was found to correlate best with significant peak steepness $H_p k_p / 2$, where

$$H_p = 4 \left[\int_{0.7f_p}^{1.3f_p} E(f) df \right]^{1/2}, \quad (9)$$

and k_p is the peak wavenumber, calculated from f_p with the deep-water dispersion relation. Another measure of steepness can be calculated using the significant wave height H_s in place of H_p . Banner et al. (2002) showed that for a range of wave scales, the breaking probability was related to the azimuthal-integrated spectral saturation:

$$\sigma = \int_0^{2\pi} k^4 \Phi(k, \theta) d\theta = \frac{(2\pi)^4 f^5 E(f)}{2g^2}, \quad (10)$$

where Φ is the wavenumber spectrum, k is the wavenumber magnitude, and θ is the direction. Breaking was found to occur above a threshold value of σ , with the breaking probability increasing roughly linearly with σ above this threshold. The saturation spectrum is related to wave mean square slope (mss) through

$$\text{mss} = \iint k^2 \Phi(k, \theta) k dk d\theta = \int \frac{2\sigma}{f} df. \quad (11)$$

Romero et al. (2012) used the $\Lambda(c)$ distributions from Kleiss and Melville (2010) to calculate a spectral $b(c)$ based on the Drazen et al. (2008) wave slope results applied to the saturation spectrum. In the present study, bulk b values are calculated for an evolving wave field to investigate possible trends with wave slope or steepness. The calculation of b or $b(c)$ requires $\Lambda(c)$ and a separate measurement of the breaking dissipation. The use of turbulent dissipation as an estimate of breaking dissipation was first utilized in Thomson et al. (2009). In the absence of in situ measurements, Gemmrich et al. (2008) and Romero et al. (2012) used indirect estimates of dissipation from wind measurements and wave spectra [i.e., the residual of Eq. (1)]. A disadvantage of this indirect method is that uncertainties in the wind parameterizations and wave measurements can lead to errors in dissipation estimates.

In the following sections, in situ and remote techniques are used to measure dissipation from breaking, wave evolution, and $\Lambda(c)$ in a young sea with strong wind forcing. In section 2, the field experiment is described and the methods are summarized. In section 3, the results are presented and in situ measurements are compared with $\Lambda(c)$ estimates. In section 4, the findings are discussed and sources of uncertainty in the data are addressed.

2. Methods

a. Collection of wind and wave data

Observations were made in the Strait of Juan de Fuca ($48^{\circ}12'N$, $122^{\circ}55'W$), north of Sequim, Washington, from 12 to 19 February 2011. Measurements were taken onboard the R/V *Robertson* and from two free-floating SWIFT drifters. The roughest conditions were observed during the days of 14 and 15 February, on which a winter storm produced southerly winds of $9\text{--}18\text{ m s}^{-1}$. On these days, the R/V *Robertson* was set on a drogue and allowed to drift across the strait (downwind) at approximately 2 km h^{-1} .

Wave measurements were made from the two wave-following SWIFT drifters. These Lagrangian drifters are described in detail in Thomson (2012). They were equipped with a Qstarz BT-Q1000eX, 5-Hz GPS logger and accelerometer, 2-MHz Nortek Aquadopp high-resolution (HR) pulse-coherent acoustic Doppler current profiler (ADCP) with 4-Hz sampling and 4-cm bin size, GoPro Hero digital video camera, and Kestrel 4500 anemometer. The SWIFTS were released from the R/V *Robertson* and generally drifted at similar speeds, thus staying within approximately 1 km of the ship. Wave frequency spectra and associated parameters are estimated from the orbital velocities measured by Doppler speed-resolving GPS loggers onboard the freely drifting SWIFTS, using the method of Herbers et al. (2012).

Wind measurements were made from a shipboard sonic anemometer (R. M. Young 8100) at a height of 8.9 m above the water surface, as well as from the SWIFTS at 0.9 m. The wind friction velocity is estimated using the inertial dissipation method as described in Yelland et al. (1994). Thomson (2012) measured the drift of the SWIFTS due to wind drag at speeds roughly 5% of the wind speed. Using this estimate to remove wind drift, the tidal surface currents can be inferred as the residual of the SWIFT displacements and were below 0.6 m s^{-1} throughout the experiment.

Figure 1 shows the tracks of the ship and SWIFTS for the two days of interest. In addition, bulk wind and wave quantities are shown as a function of fetch. Wave height and period increased along track, and wind speed

increased slowly on both days. Wind friction velocity, however, did not vary as much as wind speed during the 2 days. The nondimensional wave age, calculated as $c_p U_{10}^{-1}$ where c_p is the peak phase speed, only briefly exceeds 0.5 at the beginning of each day, when the wind is lowest. Thus, the observed waves constitute a young, highly forced, and pure wind sea.

In addition, wind measurements are used from two nearby stations operated by the National Data Buoy Center (NDBC), with locations shown in Fig. 1a. The anemometer at Smith Island (NDBC SISW1) is located at 17.1 m above the site elevation, or 32.3 m above the mean sea level. The 3-m discus buoy offshore of the Dungeness Spit (NDBC 46088) makes wind measurements from a height of 5 m above sea level. Additionally, the Dungeness buoy outputs frequency directional wave spectra.

Figure 2 shows the evolution of the SWIFT-derived wave frequency spectrum binned by fetch every 500 m. It has been widely observed that the spectrum approaches a region of the form f^{-n} for high frequencies, with the most commonly cited values of n being $n = 5$ (as in Phillips 1958; Hasselmann et al. 1973) and $n = 4$ (as in Toba 1973; Donelan et al. 1985), both of which are shown in Fig. 2. In deriving Eq. (6), Phillips (1985) used the Toba (1973) form $E(f) \propto u_* g f^{-4}$, so this comparison is of particular interest. Except for briefly after the peak and in the higher frequencies ($f \geq 1\text{ Hz}$), the spectra follow f^{-5} much better than f^{-4} . When colored by u_* in Fig. 2b, however, the curves do appear to sort in the tail as expected from the Toba spectrum.

b. In situ estimates of energy dissipation

The rate of energy dissipation via wave breaking is estimated using in situ measurements of turbulent velocity profiles $u(z)$ in a reference frame moving with the wave surface. This is done from two SWIFT drifters, as described above and in Thomson (2012) and, independently, from a wave-following platform equipped with SonTek DopBeam pulse-coherent acoustic Doppler profilers and tethered to the ship with a 30-m rubber cord. This DopBeam system is discussed further in Gemmrich (2010).

The volumetric dissipation rate $\epsilon_{vol}(z)$ is calculated by fitting a power law to the observed turbulent structure function:

$$D(z, r) = \langle [u'(z) - u'(z + r)]^2 \rangle = A(z)r^{2/3} + N, \quad (12)$$

where z is measured in the wave-following reference frame (i.e., $z = 0$ is the water surface), r is the lag distance between measurements (corresponding to eddy scale), $A(z)$ is the fitted parameter, N is a noise effect, and the

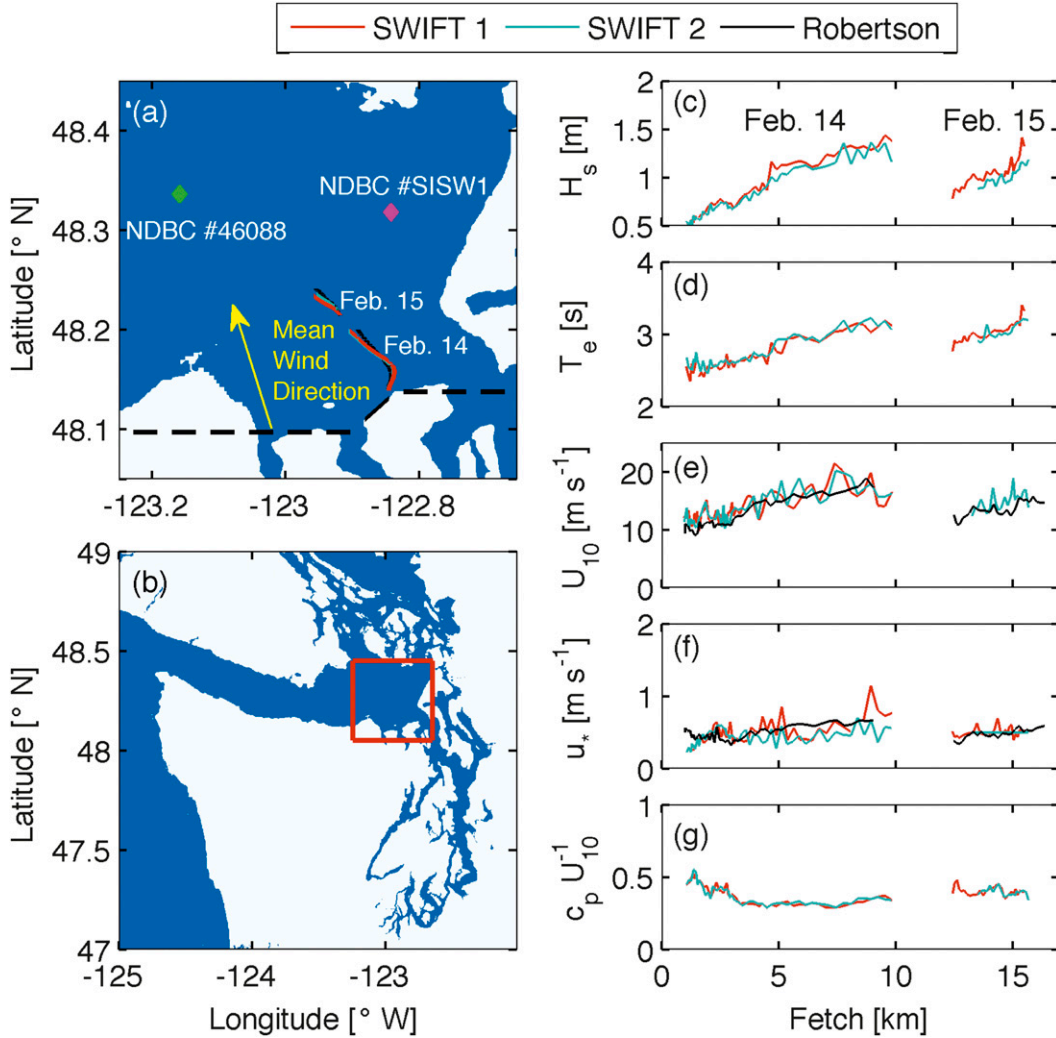


FIG. 1. (a) Instrument and ship tracks during 14 and 15 Feb. The dashed line is the zero-fetch line. The solid lines are the tracks of the R/V *Robertson* and DopBeam (black), SWIFT 1 (red), and SWIFT 2 (cyan). The yellow arrow shows the average direction of the wind from both days. (b) Map of the Pacific Northwest showing the Strait of Juan de Fuca. The red box corresponds to the edges of (a). (c)–(g) Evolution of the wave and wind conditions with fetch measured from SWIFT 1 (red), SWIFT 2 (cyan), and the R/V *Robertson* (black line in wind measurements). Conditions shown are significant wave height (c), peak energy period (d), 10-m wind speed (e), friction velocity (f), and wave age (g).

angle brackets imply a time average (5 min in this case). Assuming isotropic turbulence in the inertial subrange, the eddy cascade goes as $r^{2/3}$ and the volumetric turbulent dissipation rate is related to each fitted $A(z)$ by

$$\epsilon_{\text{vol}}(z) = C_v^{-3} A(z)^{3/2}, \quad (13)$$

where C_v is a constant equal to 1.45 (Wiles et al. 2006). Integrating the dissipation profiles over depth gives a total dissipation rate

$$S_{\text{ds,SWIFT}} = \rho_w \int_{-0.6}^0 \epsilon_{\text{vol}}(z) dz, \quad (14)$$

where z is measured from the instantaneous water surface ($z = 0$) to the bottom bin depth of 0.6 m. The structure function is averaged over 5-min intervals before calculating the dissipation. In addition, profiles of $\epsilon_{\text{vol}}(z)$ are removed if the $r^{2/3}$ fit does not account for at least 80% of the variance or if A is similar in magnitude to N (see Thomson 2012). Figure 3 shows the evolution of the dissipation profiles and total dissipation with fetch. Profiles of dissipation deepen, and the overall magnitude increases as waves grow along fetch and breaking increases. In Thomson et al. (2009), a persistent, constant background dissipation of 0.5 W m^{-2} was noted in both Lake Washington and Puget Sound in the

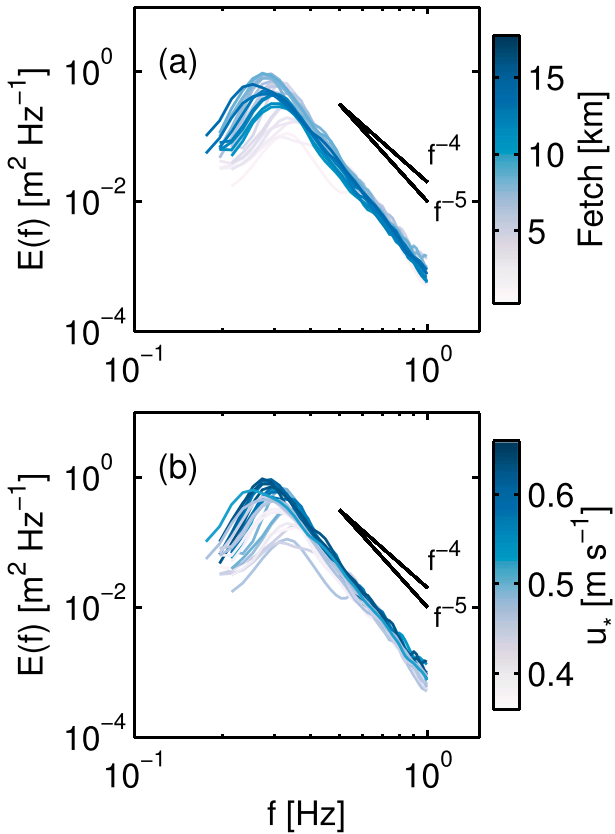


FIG. 2. Wave frequency spectra colored by (a) fetch and (b) u_* . Also shown are power laws of the form f^{-4} and f^{-5} .

absence of visible breaking. This is consistent with the SWIFT measurements here; thus, a 0.5 W m^{-2} average background dissipation level is subtracted from SWIFT and DopBeam dissipation measurements in the following sections.

c. Video observations of wave breaking

Wave breaking observations were made from a video camera mounted above the R/V *Robertson* wheelhouse, at 7 m above the mean water level, aimed off the port side of the ship. With the drogue set from the stern, the port side view was an undisturbed wave field. The video camera was equipped with a $\frac{1}{3}$ " high-resolution Sony ExView black and white charge-coupled device (CCD). The data [eight-bit grayscale, 640×480 pixel, National Television System Committee (NTSC)] were sampled at 30 Hz and later subsampled to 15 Hz. The lens had a 92° horizontal field of view and was oriented downward at an incidence angle of approximately 70°, giving a pixel resolution of 10–40 cm in the analyzed region. The video was stabilized in the vertical and azimuthal (pitch and yaw) directions with a pan-tilt mounting system (Directed

Perception PTU-D100). These video data are used to estimate the breaking rates and the $\Lambda(c)$ distributions.

Additionally, video taken from the SWIFTS is examined to produce independent estimates of the rate of breaking at a much higher pixel resolution (because the SWIFT cameras are only 0.9 m from the surface). Unfortunately, the batteries on the SWIFT GoPro cameras expired after around 2 h, so only early conditions on each day could be examined. A total of 11 30-min video recordings from the SWIFTS are processed. SWIFT breaking rates are calculated by counting the number of breaking waves passing the SWIFT and dividing by the duration of the recording (30 min). The counting is subjective, as the SWIFT video is too motion contaminated to produce accurate automated results. Only clear whitecaps that broke prior to reaching the SWIFT with crest lengths larger than the diameter of the SWIFT hull (0.3 m) are counted.

Shipboard video data are processed according to Thomson and Jessup (2009), as summarized below. Four minor modifications to this method are detailed in the appendix.

The analysis begins with the rectification of camera pixels to real-world coordinates using the method of Holland et al. (1997). Here, the x and y directions are taken as the along- and cross-ship directions, respectively. A portion of the image, roughly $15 \text{ m} \times 20 \text{ m}$ and no closer than 15 m from the ship, is extracted and interpolated to a uniform grid of 2^n points. The camera position was remotely reset periodically, as it was prone to drift in the azimuth at a rate of about 5° min^{-1} . Short video windows of 5–10 min were chosen for analysis to avoid these resets and ensure statistical stationarity of the breaking conditions. This window length is comparable to those shown in Kleiss and Melville (2010), although the field of view is significantly smaller (roughly 0.2 km^2 in their study). The uncertainty introduced from these small windows is addressed in section 4. This field of view is sufficient to capture complete crests for the conditions observed. The resulting pixel resolution is around 0.25 m (cross wave) $\times 0.075 \text{ m}$ (along wave).

The rectified video is broken up into segments of 1024 frames (68.3 s) with 25% overlap. Sequential images are subtracted to create differenced images, which highlight the moving features of the video, most prominently the leading edge of breaking waves. The breaking crests are further isolated when the differenced images are thresholded to binary images $I(x, y, t)$ (see the appendix for choice of threshold). This procedure was originally described in Gemmrich et al. (2008). Two examples of the progression from raw image to binary are shown in Fig. 4 along with SWIFT images from the same times. These images demonstrate the range of breaking conditions seen

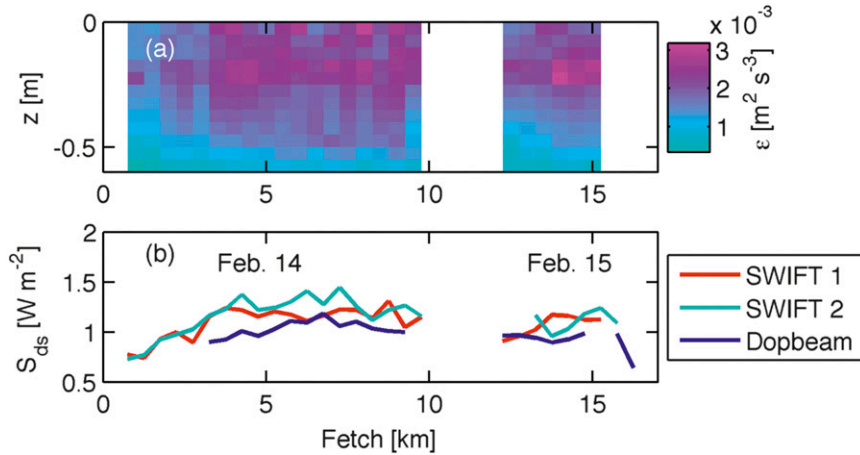


FIG. 3. (a) Turbulent dissipation profiles from SWIFT 1 plotted with fetch. Depth is measured from the instantaneous sea surface. (b) Total (integrated) turbulent dissipation measured by SWIFT 1 (red), SWIFT 2 (cyan), and DopBeam system (blue) vs fetch, averaged over 500 m. The background dissipation level of 0.5 W m^{-2} has not been subtracted from these values but is shown as the lower axis limit of (b).

during the experiment. The left images are representative of the calmer conditions toward the beginning of both days' experiments, with small and transient breaking crests. The right images are representative of the rough conditions later in each day (after drifting out to a larger fetch), with larger and more vigorous breaking crests.

After thresholding, a three-dimensional fast Fourier transform (FFT) is performed on the binary shipboard video data $I(x, y, t)$, which is then filtered in wavenumber to isolate the crest motion. Integration over the k_y (along crest) component produces a two-dimensional frequency-wavenumber spectrum $S(k_x, f)$, as shown in Fig. 2a of Thomson and Jessup (2009). Directional distributions of breaking could not be calculated from this dataset because of the shipboard camera configuration. With a camera height of 7 m and incidence angles of 60° – 70° , changes in sea surface elevation due to the waves themselves can manifest as movement in the lateral, or y , direction. This corrupts the y velocities and prevents the calculation of an accurate directional distribution. Following the method of Chickadel et al. (2003), the frequency-wavenumber spectrum is transformed to a speed-wavenumber spectrum using $c = f/k_x$, and the Jacobian $|\partial f/\partial c| = |k_x|$ preserves the variance in the spectrum. The speed spectrum is calculated by integrating over the wavenumber, $S(c) = \int S(k_x, c) dk_x$. This speed spectrum has the shape of the $\Lambda(c)$ distribution, but it must be normalized to have the correct magnitude. The normalization follows from a direct calculation of the average breaking length per unit area:

$$L_{\text{total}} = dy \frac{\sum I(x, y, t)}{NA}, \quad (15)$$

where dy is the length of the pixels along the crests, $\sum I(x, y, t)$ is the number of breaking pixels, N is the number of frames, and A is the area of the field of view. Thus, $\Lambda(c)$ is calculated as

$$\Lambda(c) = L_{\text{total}} \frac{S(c)}{\int S(c) dc}, \quad (16)$$

directly following Thomson and Jessup (2009). The removal of bias in Eq. (16) is described in the appendix.

There were 9 cases of 5–10 min used from the video record to calculate $\Lambda(c)$ distributions during the experiment. Table 1 shows the time, fetch, duration, and bulk wind and wave values from these cases. Figure 5 shows the resulting $\Lambda(c)$ as a function of dimensional speed and normalized speed c/c_p and colored by mss. These distributions are qualitatively similar to those from Gemmrich et al. (2008), Thomson et al. (2009), and Kleiss and Melville (2010), with a peaked shape centered at approximately $0.5c_p$. As expected, the magnitude of $\Lambda(c)$ increases with mss. In addition, a region of roughly c^{-6} is visible at high speeds, similar to the theoretical shape described in Eq. (8).

3. Analysis and results

a. Fetch dependence

The R/V *Robertson* and SWIFT measurements of winds and waves are highly dependent on fetch because of the drift mode for data collection. The fetch dependence is directly related to wave slope and thus wave

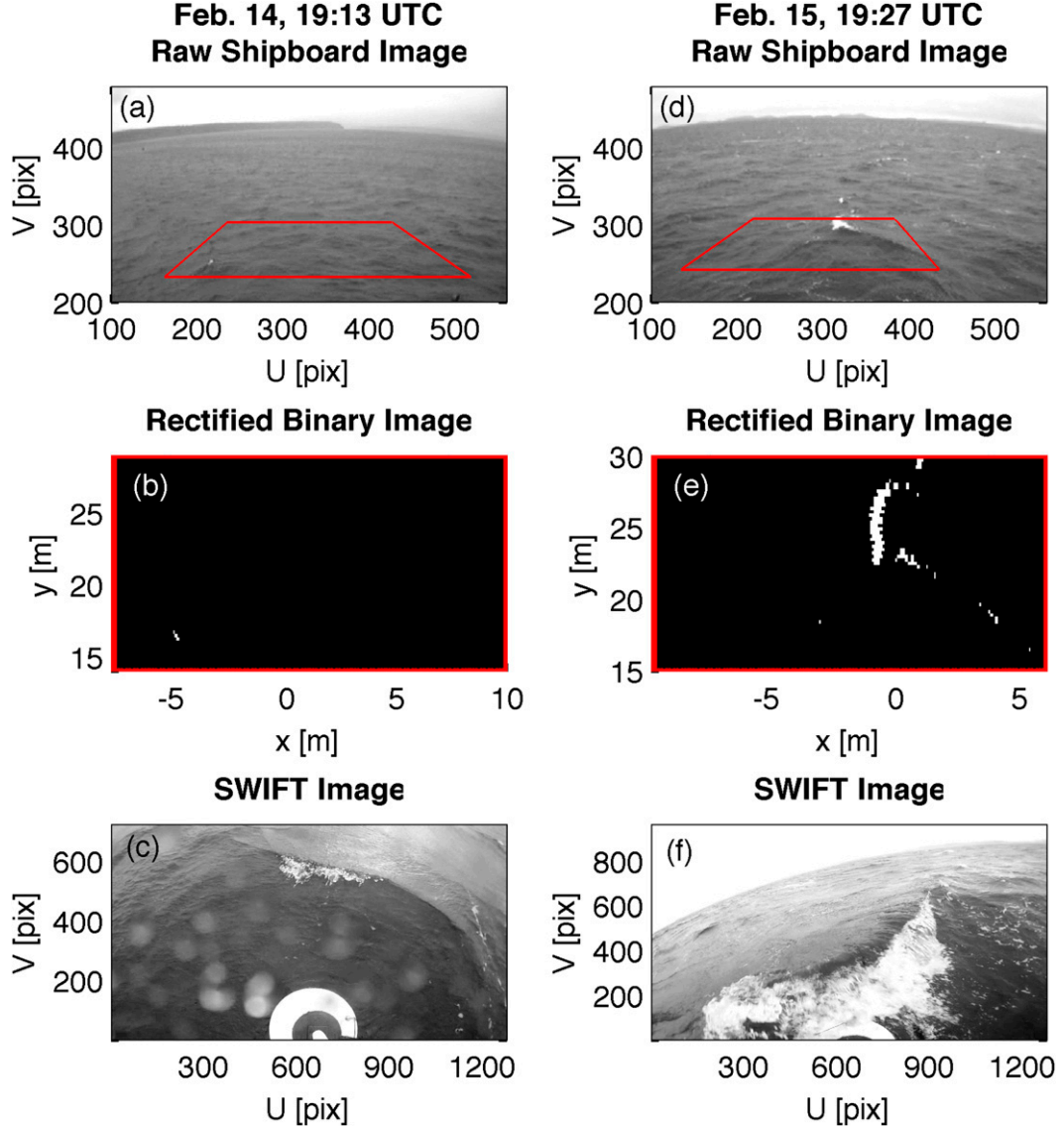


FIG. 4. Sample images of breaking from shipboard and SWIFT video. Images are taken from (a)–(c) 19:13 UTC 14 Feb, during calmer wave conditions, and (d)–(f) 19:27 UTC 15 Feb, during steeper wave conditions. Raw, stabilized shipboard images, with the red box showing the sampled field of view are given in (a),(d); the corresponding thresholded, binary images in rectified real-world coordinates are given in (b),(e); and sample SWIFT images from coincident times (i.e., not identical waves) are given in (c),(f).

breaking (Banner et al. 2002). Here, these measurements are compared with the idealized case of fetch-limited wave growth, in which a wind of constant magnitude and direction blows out from a straight coastline.

Figure 6 compares the drifting measurements of wind speed, direction, and wave height from the R/V *Robertson* and SWIFTS with fixed measurements from the two nearby NDBC stations (see locations in Fig. 1). The NDBC measurements are converted to U_{10} by assuming a logarithmic profile with a representative drag coefficient $C_D = 1.2 \times 10^{-3}$ (Large and Pond 1981).

There is significant spatial heterogeneity in the wind speed measurements. In particular, on 14 February the wind measured from the ship increases dramatically with increasing fetch, while both NDBC wind speed measurements are roughly constant. The ship wind speeds converge to roughly the same 17 m s^{-1} value as measured from the NDBC stations when the ship reaches a fetch similar to the NDBC stations. It is likely that some of the increase in measured wind speed with fetch is due to the sharp transition in roughness at the coastline and the resulting adjustment of the boundary layer

TABLE 1. Time/date, duration, and fetch of the nine $\Lambda(c)$ observations. Also shown are the bulk wave and wind quantities, calculated as 500-m averages around each point in fetch.

Time/date	Duration (min)	Fetch (km)	H_s (m)	T_e (s)	U_{10} ($m s^{-1}$)	u_* ($m s^{-1}$)
19:10 UTC 14 Feb 2011	6.8	1.40	0.56	2.55	9.74	0.45
20:36 UTC 14 Feb 2011	6.5	3.01	0.71	2.61	11.50	0.37
20:48 UTC 14 Feb 2011	5.1	3.37	0.76	2.64	12.55	0.42
21:34 UTC 14 Feb 2011	6.5	5.24	1.08	2.89	15.07	0.56
21:41 UTC 14 Feb 2011	8.5	5.60	1.12	2.97	15.73	0.60
22:27 UTC 14 Feb 2011	6.0	8.33	1.26	3.11	17.24	0.64
22:35 UTC 14 Feb 2011	4.8	8.84	1.29	3.14	18.01	0.66
19:04 UTC 15 Feb 2011	10.0	12.55	0.86	2.87	11.45	0.36
19:27 UTC 15 Feb 2011	6.0	13.17	1.00	2.97	13.11	0.48

(Smith and Macpherson 1987). The 15 February wind data, measured only at fetches longer than 12 km, matches the NDBC measurements much better. As expected, the wave height at the NDBC buoy stays approximately constant in response to the roughly steady winds, whereas the SWIFT wave heights grow in time due to the increasing fetch along a drift track.

For ideal fetch-limited waves, Kitaigorodskii (1962) argued that the wave field could be fully characterized by the fetch X , gravitational acceleration, and a scaling wind speed. Thus, empirical “laws” have often been sought for wave energy and frequency growth with fetch (e.g., CERC 1977; Donelan et al. 1985; Dobson et al. 1989; Donelan et al. 1992). The scaled variables take the form

$$\hat{x} = \frac{gX}{U_{10}^2}, \quad \hat{e} = \frac{g^2 E_0}{U_{10}^4}, \quad \text{and} \quad \hat{f} = \frac{U_{10} f_p}{g}, \quad (17)$$

where E_0 is the wave variance, and f_p is the frequency at the peak of the wave spectrum. The wind speed at a 10-m reference height U_{10} is most often used as the scaling wind speed as it is easily measured in the field. Young (1999) consolidated a number of the proposed fetch relations into two power laws with a range of coefficients. Figures 7a and 7b compare this current dataset against Young’s empirical relations, using 500-m along-fetch averaging.

The nondimensionalized data are highly sensitive to the choice of appropriate wind speed, particularly for 14 February where the wind grows from 10 to 19 $m s^{-1}$ along the fetch. Three wind speed scalings are compared in Figs. 7a and 7b, using a constant time-averaged wind speed, an instantaneous wind speed, and a linear fetch-averaged wind speed (as in Dobson et al. 1989). Based on the NDBC wind data alone, a constant U_{10} scaling might seem appropriate. In fact, scaling with the constant wind agrees much better with the empirical fetch laws than either fetch-dependent wind speed scaling. In addition, wave conditions at the Dungeness Spit buoy (NDBC 46088) are also plotted in Figs. 7a and 7b, and

there is good agreement with the fetch laws. This is a notable contrast of reference frames: the fixed station suggests a fetch-limited wave field, while the drifting measurements do not.

Two additional parameters are plotted against non-dimensional fetch in Figs. 7c and 7d. One is mss calculated from the wave spectra as in Eq. (11), which is associated with the likelihood of wave breaking (Banner et al. 2002). Wave slope increases logarithmically with nondimensional fetch on 14 February. On 15 February, mss also increases with fetch, but the waves are in the midrange of the previous day. These trends are similar for a number of alternative slope or steepness parameters (not shown). Also plotted is the drag coefficient, calculated as a ratio of u_*^2 and U_{10}^2 . These measurements are independent, because u_* is calculated from wind turbulent dissipation (Yelland et al. 1994) rather than mean wind speed. At very short fetches, the drag is notably higher than the remainder of the data, which again is evidence of the adjustment of the atmospheric boundary layer to the land–water edge. At longer fetches, drag is in the expected range from 1×10^{-3} to 2×10^{-3} and shows a mild increasing trend along fetch (and thus with steepness).

This field experiment exhibits two of the features—an irregular coastline and wind heterogeneity—which prompted Donelan et al. (1992) to write that “perhaps it is time to abandon the idea that a universal power law for non-dimensional fetch-limited growth rate is anything more than an idealization.” It is likely that the ambiguous comparison of the data with the established fetch laws is a result of both the nonideal winds and the rapid change of the atmospheric boundary layer at very short fetches, which itself is a result of changes in roughness due to waves. The observed fetch dependence suggests a wave field that rapidly evolves in the first few kilometers, and then grows more gradually as the fetch lengthens. This is consistent with the in situ breaking dissipation estimates, which increase sharply from 0- to 5-km fetch, then vary only moderately from 5- to 15-km fetch (Fig. 3).

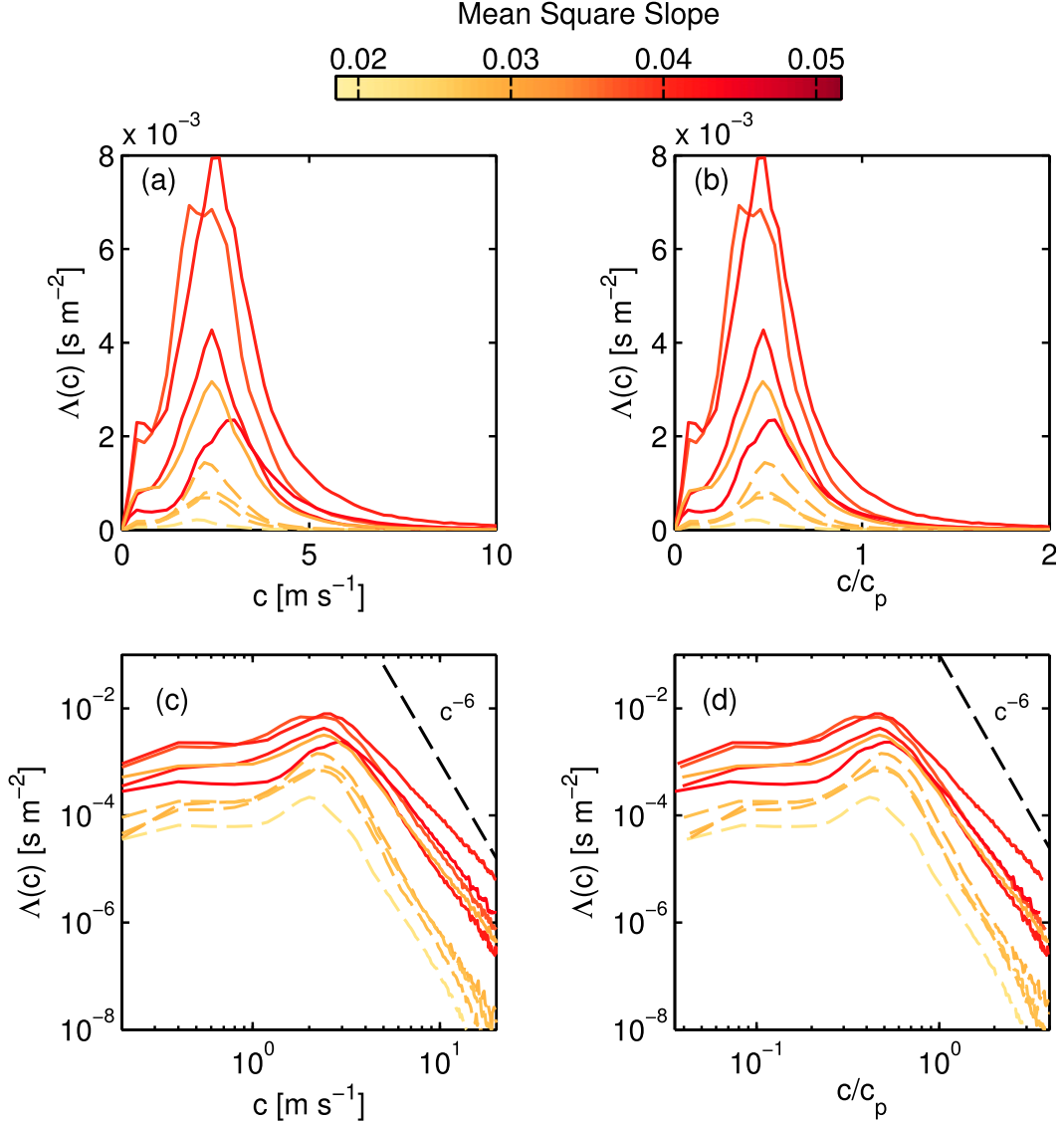


FIG. 5. $\Lambda(c)$ vs (a),(c) dimensional and (b),(d) nondimensional phase speed, in linear (a),(b) and logarithmic (c),(d) coordinates. All curves colored by mss. Dashed curves are $\Lambda(c)$ results shown to be biased low by comparison with SWIFT breaking rate estimates. Black dashed line is the c^{-6} power law derived in Phillips (1985).

b. Energy fluxes

As discussed in section 1, the evolution of ocean surface waves is governed by RTE. Here, we calculate each of the terms in a bulk RTE, which is integrated over all frequencies:

$$\frac{\partial E}{\partial t} + (\mathbf{c}_g \cdot \nabla) E = S_{in} - S_{ds}, \quad (18)$$

such that the nonlinear term is dropped as it does not change the total energy in the system, only the distribution of the energy within the spectrum. By considering the total energy budget, we can diagnose the wave

evolution along fetch and assess the estimates of wave breaking dissipation. Figure 8 shows the estimates of all terms in Eq. (18).

In general, both local growth and advective flux of wave energy [the left two terms in Eq. (18)] occur in response to wind forcing. Without a large array of wave measurements, it is impossible to explicitly separate the two growth terms. One approximation is to assume a stationary wave field, such that $\partial E/\partial t = 0$ and all wave growth is due to the advection of wave energy at the group velocity. The ambiguous comparison with empirical fetch laws in Fig. 7, however, indicates that a stationary assumption may not be appropriate. An

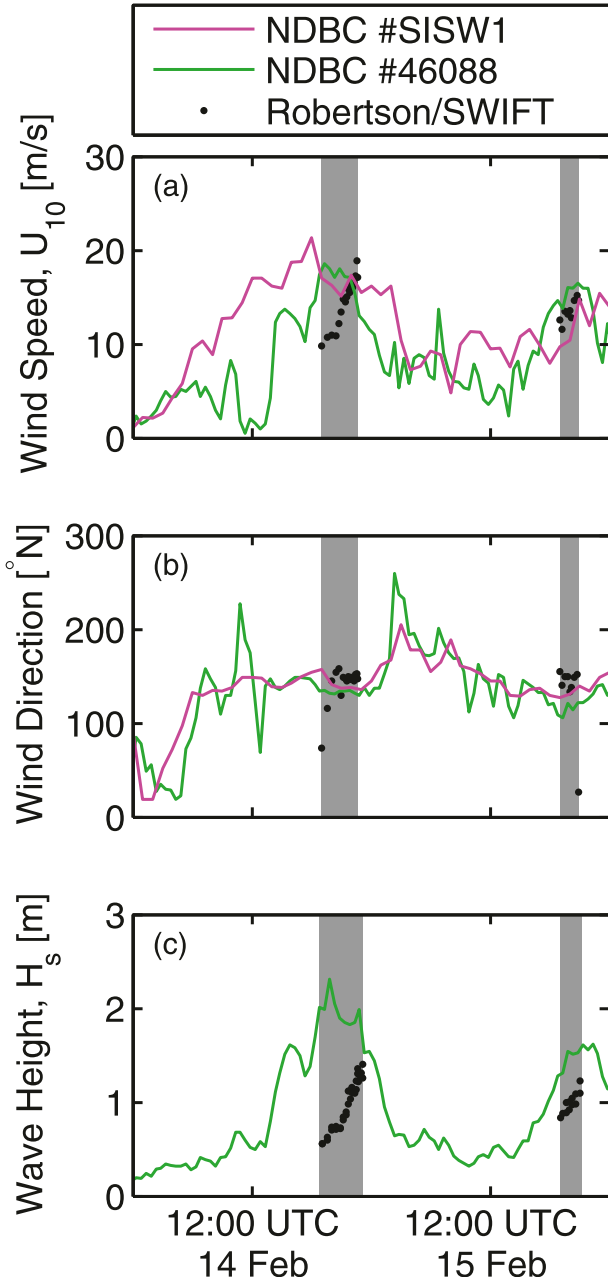


FIG. 6. Time series of (a) U_{10} , (b) wind direction, and (c) significant wave height H_s from nearby NDBC stations: the Smith Island Meteorological Coastal-Marine Automated Network (C-MAN) station (SISW1, magenta) and the New Dungeness 3-m discus buoy (46088, green). Black points are experimental values measured from the R/V *Robertson* (a),(b) and SWIFTS (c).

additional issue is noise in the wave energy measurements, which causes large variability in the growth terms when using finite differences to approximate the derivatives. This is problematic even when the spectra are averaged over 500-m spatial bins as in Fig. 2.

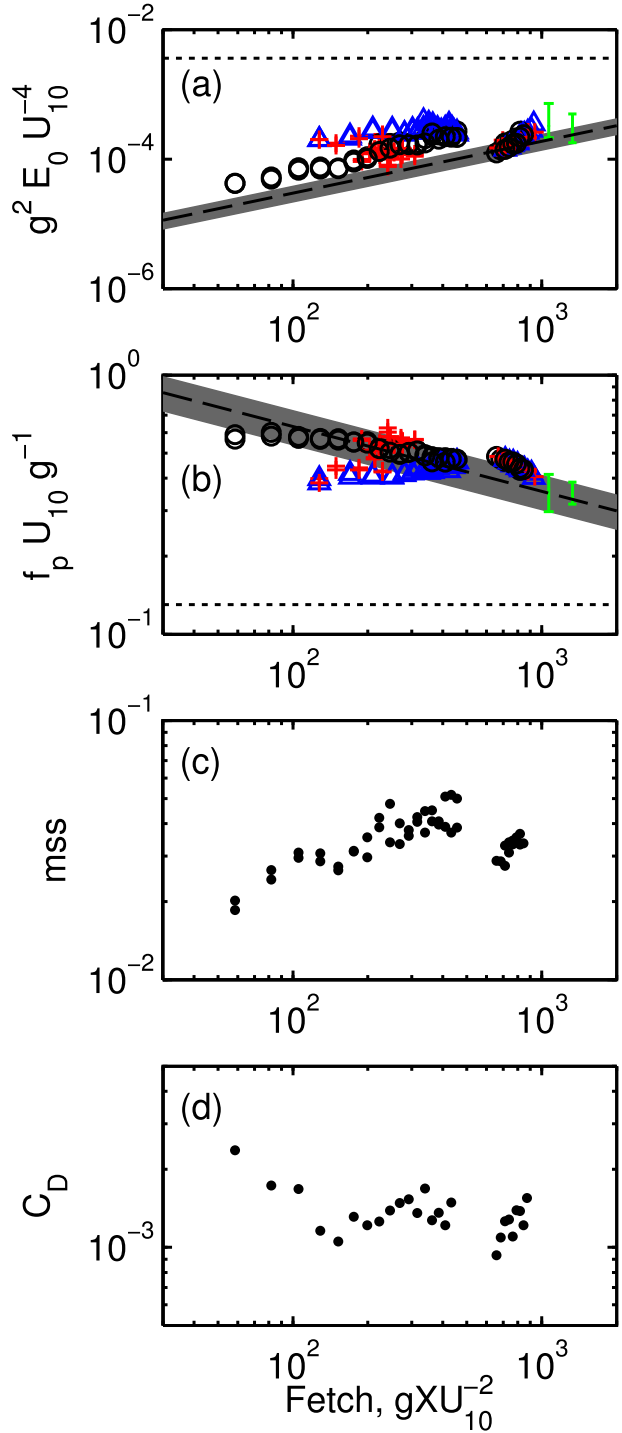


FIG. 7. Evolution of four wave parameters plotted against non-dimensional fetch. (a) Nondimensional wave energy. Black circles use the mean daily wind speed, blue triangles use a linear fetch-integrated wind speed, and red crosses use the instantaneous wind speed. Green symbols show the values from the NDBC 46088 wave buoy, taken from the shaded areas on Fig. 6, with error bars for the min and max of the range of values. The Young (1999) empirical relation is shown by the black dashed line with gray range of parameters and fully developed limits (horizontal solid black line). (b) Non-dimensional frequency, symbols as in (a), (c) mss, and (d) C_D .

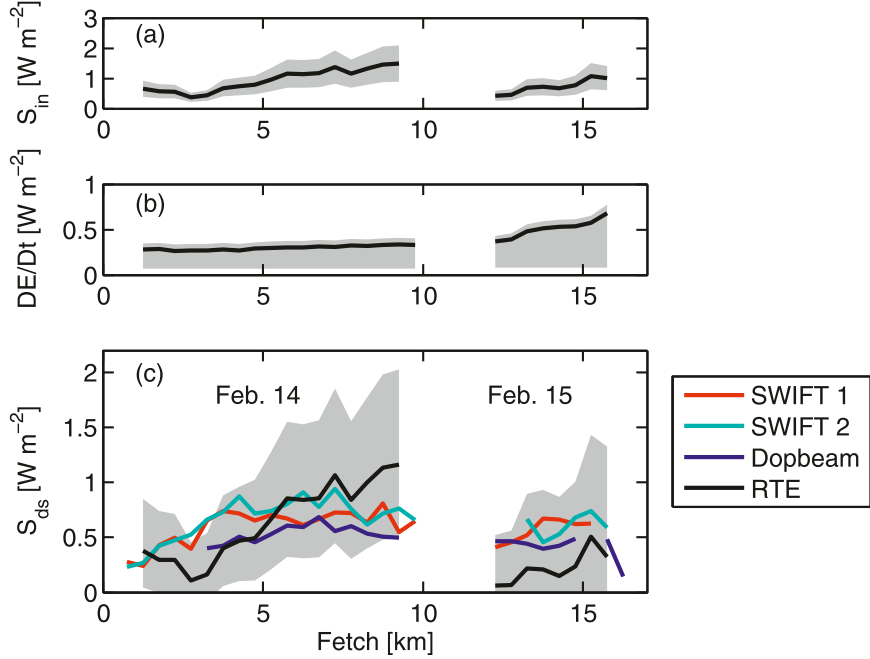


FIG. 8. Evaluation and comparison of wave fluxes. Gray shaded regions show possible range of (a) wind input, (b) wave energy flux, and (c) breaking dissipation vs fetch. Black lines come from a stationary assumption $\partial E/\partial t = 0$ and using the mean value of $c_{\text{eff}} = 0.5$. Colored curves of dissipation are calculated directly from turbulent dissipation for SWIFT 1 (red), SWIFT 2 (cyan), and DopBeam (blue), with a background dissipation level of 0.5 W m^{-2} subtracted off. All quantities are 500-m averages.

To treat both the issues of stationarity and measurement noise in the left-hand side of Eq. (18), large-scale estimates are made separately based on daily linear regressions of wave energy with fetch and time (i.e., regressions of ΔE versus Δx and Δt). The first case is equivalent to the stationary assumption, where all growth during the experiment is due to the advection of wave energy. In the second case, the wave energy is assumed constant in fetch, such that all the change in wave energy is due to local, temporal growth. Tables 2 and 3 show the results of $\partial E/\partial t$ and $\partial E/\partial x$ for 14 and 15 February, including R^2 values and 95% confidence intervals (CI). As noted above, neither of these cases describes perfectly the true evolution of wave energy, which is actually a combination of both terms. However, they lead to a range of possible values

$$\min\left(\overline{\frac{\partial E}{\partial t}}, c_g \overline{\frac{\partial E}{\partial x}}\right) \leq \left(\frac{\partial E}{\partial t} + c_g \frac{\partial E}{\partial x}\right) \leq \left(\overline{\frac{\partial E}{\partial t}} + c_g \overline{\frac{\partial E}{\partial x}}\right), \quad (19)$$

where overbars indicate the daily averages from Tables 2 and 3. Here, one-dimensional advective wave growth is assumed, with c_g calculated from the peak frequency using the deep-water dispersion relation.

Figure 8b shows this range of values from Eq. (19). Apart from the small change in c_g , this estimate does not capture possible variations in growth within each day, but the R^2 values shown in Tables 2 and 3 show that a constant linear approximation is reasonable (minimum R^2 of 0.82, mean of 0.90). A more conservative range would use the outer values of the 95% confidence intervals of the regressions.

The wind input function in Eq. (18) is parameterized using the wind stress $\rho_a u_*^2$ and an effective phase speed c_{eff} , such that

$$S_{in} = \rho_a c_{\text{eff}} u_*^2, \quad (20)$$

as described in Gemmrich et al. (1994). There is significant uncertainty in the choice of c_{eff} . Terray et al. (1996) found c_{eff} to be somewhat less than the peak phase speed and show a dependence on wave age, albeit with much scatter. Figure 6 from Terray et al. (1996) shows values of c_{eff} ranging between roughly $0.3c_p$ and $0.7c_p$ for our range of $u_* c_p^{-1}$. Thus, the range of values for the wind input term is

$$0.3\rho_a c_p u_*^2 \leq S_{in} \leq 0.7\rho_a c_p u_*^2. \quad (21)$$

The resulting wind input range is shown in Fig. 8a.

TABLE 2. Linear fits of the daily wave energy growth with fetch for SWIFTs 1 and 2. When multiplied by c_g , $\overline{\partial E/\partial x}$ gives an estimate of the advective wave growth. The intercept indicates the value of fetch for which the linear fit extrapolates to give zero wave energy. The R^2 values and 95% confidence intervals (W m^{-3}) are also shown.

Day	SWIFT	$\overline{\partial E/\partial x}$	Intercept	R^2	95% CI (W m^{-3})
		(W m^{-3})	(km)		
14 Feb	1	0.125	-0.23	0.951	$\pm 1.51 \times 10^{-2}$
14 Feb	2	0.111	-0.41	0.931	$\pm 1.60 \times 10^{-2}$
15 Feb	1	0.152	9.46	0.926	$\pm 4.95 \times 10^{-2}$
15 Feb	2	0.230	11.97	0.852	$\pm 1.33 \times 10^{-1}$

With Eqs. (18), (19), and (21), the range of possible dissipation values during the experiment can be computed and compared with the measured turbulent dissipation from the SWIFTs and DopBeams. This comparison is shown in Fig. 8c. An additional black line is shown in each of the panels, corresponding to $c_{\text{eff}} = 0.5c_p$ and a stationary wave field ($\partial E/\partial t = 0$). The measured results fall within the estimated range from the energy balance for all but a few points during the experiment. Where this range would include negative values of dissipation, including all of 15 February, it has been limited to zero.

Whereas the stationary RTE dissipation roughly matches the turbulent dissipation on 14 February, it underestimates the turbulent dissipation on 15 February, consistent with an overestimate of $\partial E/\partial x$. This is related to the intercept of the linear regression in fetch (see Table 2). If the growth were perfectly linear in fetch, this intercept would be expected to be near zero (no wave energy at zero fetch). On 14 February, this is indeed the case, with the intercept at less than 1 km. On 15 February, however, the intercept is on the order of 10 km, indicating that either the growth is not linear along fetch or the growth is not steady. This is consistent with Fig. 7, where for all wind speed scalings, wave energy on 15 February grows faster than the expected trend.

Figure 8 shows that bulk dissipation estimates from the RTE are similar to turbulent dissipation measurements, both of which show dissipation increasing along fetch (and thus with wave slope), especially at very short fetches. At larger fetches, the RTE dissipation continues to increase, more so than the relatively flat turbulent dissipation measurements. It is likely that the in situ turbulence measurements of dissipation are biased low because some wave energy is lost during whitecapping to work in submerging bubbles (Loewen and Melville 1991). Thus, if bubble effects account for an increasing fraction of the total dissipation as the waves grow, the turbulence measurements would increasingly underestimate the total dissipation, as seen particularly on 14 February. This is

TABLE 3. Linear fits of the daily wave energy growth with time for SWIFTs 1 and 2. For each day, $\overline{\partial E/\partial t}$ gives an estimate of the temporal wave growth. The R^2 values and 95% confidence intervals (W m^{-2}) are also shown.

Day	SWIFT	$\overline{\partial E/\partial t}$ (W m^{-2})	R^2	95% CI (W m^{-2})
14 Feb	1	0.075	0.915	$\pm 1.21 \times 10^{-2}$
14 Feb	2	0.067	0.873	$\pm 1.35 \times 10^{-2}$
15 Feb	1	0.065	0.955	$\pm 1.63 \times 10^{-2}$
15 Feb	2	0.093	0.816	$\pm 6.13 \times 10^{-2}$

important context for the comparison of in situ results with breaking statistics from the video data.

c. Breaking rate

Breaking rates from the ship-based $\Lambda(c)$ distributions and from the manual SWIFT-based breaker counts are shown in Fig. 9a. Both measurements show an overall positive trend with wave slope, as expected, but the dynamic range and shape of the trends are significantly different. Whereas the SWIFT values vary from only 16 to 58 h^{-1} , the shipboard breaking rates vary over two orders of magnitude, from 3 to 229 h^{-1} . Unfortunately, SWIFT video cameras ran out of battery power prior to reaching the maximum breaking conditions. The actual overlap is with the first three shipboard observations from 14 February and the first two from 15 February. In general, the SWIFT breaking rates are larger than the shipboard measurements, and thus the overall trend with mss is decreased. The low breaking rates from the shipboard video are likely biased by insufficient pixel resolution, and these values are plotted with open symbols to reflect low confidence in these points (see Fig. 9 and again later in Fig. 10). The two estimates are relatively close for the maximum overlapping point (68 h^{-1} from shipboard vs 58 h^{-1} from the SWIFT), indicating that these estimates may be consistent when the waves are larger and steeper (i.e., at larger mss in Fig. 9 and larger fetch in Fig. 8).

The SWIFT breaking rates imply that the shipboard video regularly misses breaking waves during less steep conditions, when whitecaps are short crested and the foam they produce is short lived. As shown with examples in Fig. 4, the small-scale breaking seen frequently in the SWIFT video (Fig. 4c) is barely visible in the shipboard video (Fig. 4b) during calmer conditions. Moreover, many uncounted wave crests appear to break without producing foam, but are visible from the SWIFT due to the layer of water sliding down their front face or ripples forming near the crest. These small-scale breakers are similar to “microbreakers,” which are a well-known phenomenon (e.g., Jessup et al. 1997). As the waves evolve, however, the character of the breaking

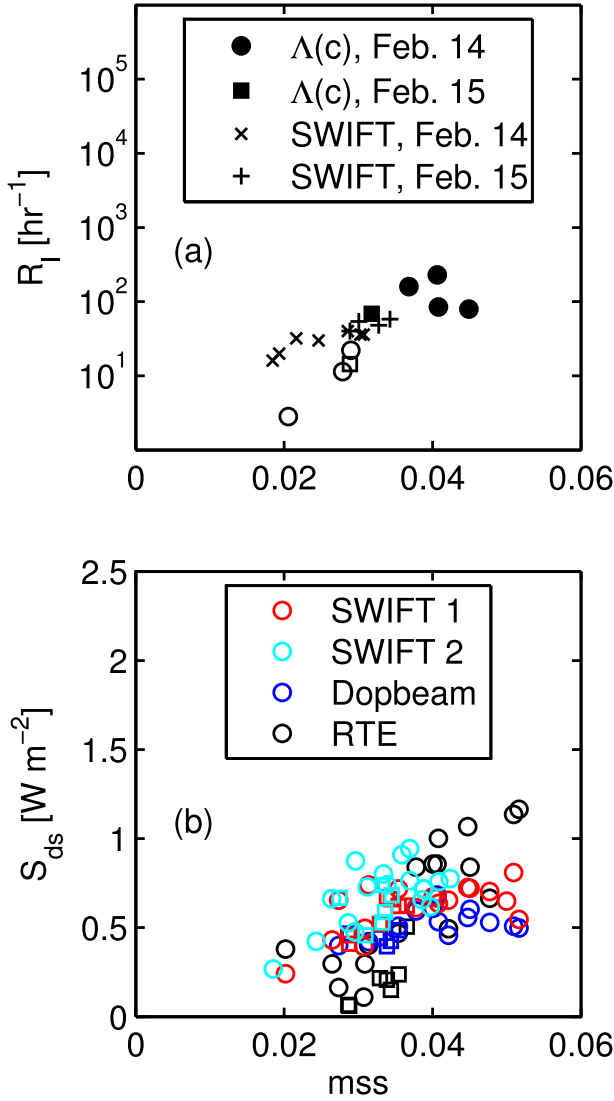


FIG. 9. (a) Breaking rate and (b) wave dissipation vs mss. Circles correspond to shipboard measurements from 14 Feb and squares are from shipboard measurements during 15 Feb in (a). Asterisks and crosses are from manual SWIFT breaking rate counts for 14 and 15 Feb, respectively. Data plotted with open symbols overlap with the SWIFT breaking rates (in time) and appear to underestimate the breaking rate. Wave dissipation from Fig. 8 is plotted vs mss for SWIFT 1 (red), SWIFT 2 (cyan), DopBeam (blue), and inferred dissipation from the RTE based on the stationary assumption (black) in (b).

changes. Large, vigorous whitecaps start to replace the small, transient breaking events seen at the shorter fetches, and evidence of microbreaking becomes less apparent. These larger whitecaps (Fig. 4f) are more visible from the shipboard video (Fig. 4d) and the breaking rates converge for later times.

The higher breaking rates from the SWIFT video during calmer conditions are consistent with the in situ

turbulent dissipation estimates. As shown in Fig. 9, both breaking and dissipation increase approximately one order of magnitude as waves evolve and steepen. This implies that each wave dissipates roughly the same amount of energy during breaking, such that more breaking produces more dissipation. The breaking rates from the shipboard video, by contrast, increase much more dramatically than the dissipation estimates, which would imply that each breaking wave contributes less dissipation as the wave field evolves. This is both physically unlikely and contrary to the Duncan–Phillips theory, where the dissipation rate of a breaking wave is proportional to c^5 times its crest length, with a proposed additional positive dependence on wave slope (Melville 1994; Drazen et al. 2008). Thus, only ship-based video recordings from the rougher conditions (filled symbols of Fig. 9a) are used in assessing the $\Lambda(c)$ and b results.

d. Breaking strength parameter

The value of the bulk breaking parameter b is calculated from

$$b = \frac{S_{ds}}{\rho_w g^{-1} \int c^5 \Lambda(c) dc}, \quad (22)$$

using each of the four measures of dissipation S_{ds} from Fig. 8. These calculated b values are shown as a function of mss, wave age, and significant steepness in Fig. 10. Only one SWIFT was in the water during the two 15 February video segments; thus, there is one less b value for these $\Lambda(c)$. The independent variables use the average of mss, c_p , U_{10} , and H_s within a 500-m region around each $\Lambda(c)$ calculation. As in Fig. 9a, values that are biased by insufficient pixel resolution are shown with open symbols.

In addition, data are included from measurements made in Lake Washington, in 2006 and Puget Sound, in 2008, originally reported in Thomson et al. (2009). Whereas in Thomson et al. (2009) a constant b was obtained via regression of $\int c^5 \Lambda(c) dc$ to the measured dissipation, here individual values of b are calculated. Apart from the updates to the Fourier method detailed in the appendix, the $\Lambda(c)$ methodology is similar between the datasets. The comparison of b with wave age and steepness is in part motivated by the desire to compare across these datasets, as the spectra from the earlier measurements are of insufficient quality to calculate mean square slope.

As expected, the b values are affected by undercounting small whitecaps in less steep seas. The biased points, shown in open symbols, have dramatic trends of decreasing b with increasing wind forcing (described by inverse wave age U_{10}/c_p) and increasing wave slope (using

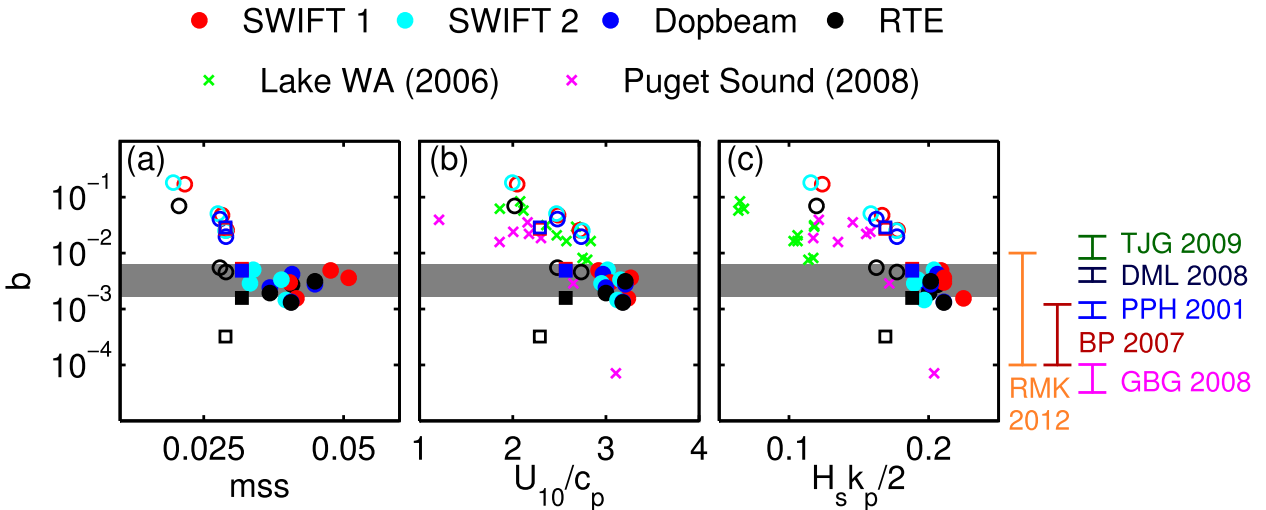


FIG. 10. Breaking strength parameter plotted vs (a) mss, (b) inverse wave age, and (c) peak steepness. Coloring as in Fig. 9b and symbols from Fig. 9a. Open symbols are used for data with known bias. Additional data from Lake Washington in 2006 (green crosses) and Puget Sound in 2008 (magenta crosses) are described in Thomson et al. (2009). Vertical bars to the right of the plots show ranges of b estimates from Thomson et al. (2009) (green), Gemmrich et al. (2008) (pink), Phillips et al. (2001) (light blue), and Banner and Pierson (2007) (dark red). For Drazen et al. (2008) (dark blue), b is extrapolated to these steepness from their power-law fit. For Romero et al. (2012) (orange), the approximate range of b for $c \leq c_p$ is shown.

mss and peak wave steepness $H_s k_p/2$). The Thomson et al. (2009) data show these same trends, suggesting the same biasing effect. This trend may be expected in any $\Lambda(c)$ study with insufficient sampling of small-scale breaking.

The remaining unbiased values, shown in solid symbols, have b grouped around a constant on the order of 10^{-3} . No statistically significant trends are present. In particular, the increase in b with wave slope shown in Drazen et al. (2008) is not observed, though the range of wave slopes here is quite limited relative to Drazen et al. (2008). Thus, as in Phillips et al. (2001), Gemmrich et al. (2008), and Thomson et al. (2009), the best estimate of b for this study is a constant range over the experimental conditions. The five unbiased $\Lambda(c)$ distributions, each paired with four S_{ds} estimates, result in an ensemble of 20 points. Among this set, the mean b value is 3.2×10^{-3} , with a standard deviation of 1.5×10^{-3} . This range is highlighted in gray in Fig. 10 and is applicable for waves with $\text{mss} \geq 0.031$ or $H_s k_p/2 \geq 0.19$.

Figure 10 also shows these b values relative to other recent studies. Clearly, they are lower than the average b from 8×10^{-3} to 20×10^{-3} reported from the Puget Sound and Lake Washington data in Thomson et al. (2009), which are a direct result of the undersampling of small breakers in the previous study. The experimental results of Banner and Pierson (2007) found laboratory waves of slope 0.12–0.17 to have b values between 1×10^{-4} and 12×10^{-4} . The laboratory study of Drazen et al. (2008) did not measure breaking waves with slopes less than 0.22, but the power law fit through their data

predicts b values between 3.1×10^{-3} and 5.3×10^{-3} for the range of steepness shown here. The Romero et al. (2012) $b(c)$ are of $O(10^{-2}-10^{-4})$ for speeds below c_p . Gemmrich et al. (2008) give a range of b that is significantly lower, $3.2 \times 10^{-5} \leq b \leq 10.1 \times 10^{-5}$. Phillips et al. (2001) calculate b ranging from 7×10^{-4} to 13×10^{-4} .

The b values reported from field studies are sensitive to the upper limit of integration in Eq. (22). This integral can be unbounded, with significant contributions to the total area coming from sporadic, extremely rare, or non-existent breaking above the spectral peak. This problem is not unique to this study, though it can be exacerbated by the Fourier method as discussed in the appendix. The results of Romero et al. (2012) suggest a solution to this dilemma. The bulk b calculated in Eq. (22) represents all speeds, in contrast to the spectral $b(c)$ from Romero et al. (2012). The Romero et al. (2012) model and data show, however, that above c_p a precipitous drop in breaking strength should be expected due to the decreased saturation of these waves. Thus, the upper limit of the integration in Eq. (22) is taken to be c_p . In effect, this amounts to a $b(c)$ model where $b(c)$ is constant for $c \leq c_p$ and zero for $c > c_p$.

4. Discussion

a. Importance of small-scale breaking

It has long been accepted that foam-based breaker detection methods are incapable of measuring microbreakers. However, microbreaking is often treated as an

afterthought, or an effect that is important only at the very short wave scales. This study leads to two important considerations regarding microbreakers. First, the distinction between whitecaps and microbreakers is not straightforward. Comparison of SWIFT and shipboard video reveals that many breaking waves that are visible from the SWIFTS do not show up in the shipboard video. These are not true microbreakers as they do aerate the surface; however, they are not visible from the ship due to their short crest length, short duration, and low contrast of foam produced. This phenomenon does not appear to be limited to the high-frequency waves; rather, it seems to be a broadband effect based more on the overall wave steepness (as given by the integrated mean square slope).

Second, these breaking waves appear to have a biasing effect. As the breaking becomes stronger, large whitecaps replace, rather than simply add to, the smaller-scale breaking events. If this biasing effect is indeed important, it is not unique to this study. Clearly, the Lake Washington and Puget Sound data from Thomson et al. (2009) shown in Fig. 10 display evidence of this bias as well. Kleiss and Melville (2011) compiled breaking rates from five datasets that show a very similar range of values to those shown here in Fig. 9, after normalizing by the wave period. Babanin et al. (2010b) compared the empirical $\Lambda(c)$ function proposed by Melville and Matusov (2002) with a numerical dissipation function and showed that b needed to change over four orders of magnitude to reproduce the appropriate dissipation. Gemmrich et al. (2008) is notable both for their low estimates of b (from $\sim 3 \times 10^{-5}$ to 10×10^{-5}) and the high resolution of their video (pixel sizes of 3.2×10^{-2} m). This is consistent with the proposition that small-scale breaking waves are not resolved in most other field measurements. Whereas Drazen et al. (2008) showed that the large range of b values reported in laboratory measurements could be somewhat explained by differences in wave steepness, we propose that the range in b reported from field measurements is large due to the biasing effect of small-scale breaking and/or the ability of different video systems to resolve small breakers.

Infrared (IR) imaging may improve remote sensing of small-scale breaking, by detecting the disturbance in the thermal boundary layer even when foam is not visible (Jessup et al. 1997). Jessup and Phadnis (2005) made IR measurements of $\Lambda(c)$ for laboratory microbreakers, but similar measurements can be challenging to make in the field. Recently, Sutherland and Melville (2013) made the first field measurements of $\Lambda(c)$ with stereo IR cameras. Such measurements are essential to quantify the dynamics of small-scale breakers and the overall effect of small-scale breaking on wave evolution.

b. Sensitivity and error in b

The largest source of uncertainty in the measured $\Lambda(c)$ is the omission of microbreakers and small-scale whitecaps. However, there are several other sources of uncertainty in the b estimates, which are shown in Fig. 11, using the S_{ds} values from SWIFT 1 (red symbols in 10).

One potential source of error is from the relatively short video recordings (5–10 min) used to determine each $\Lambda(c)$. Synthetic data were created to determine the errors of the Fourier method caused by short recordings. The synthetic data are a binary time series resembling thresholded, natural crests. The speed of the breaking crests follow a normal distribution centered around 3 m s^{-1} for similarity with the field data. Noise, in the form of randomness in the speed of each synthetic pixel, is added to avoid “ringing” in the Fourier result. In natural data, there is always sufficient noise to avoid ringing. Because the speed and crest length of the synthetic breakers is prescribed, the true $\Lambda(c)$ distribution is easily calculated and compared with the curve obtained from the Fourier method. For each video recording from the field, 50 runs of synthetic data were analyzed using the same configuration, breaking rate, and duration. An example of the family of resulting $\Lambda(c)$ distributions is shown in Fig. 12a for the data point of 21:34 UTC 14 February (see Table 1), along with the input Gaussian distribution. Clearly, significant errors from the true $\Lambda(c)$ are possible when using such limited data. The resulting uncertainty in b from propagating these errors through in the integral of $c^5 \Lambda(c) dc$ is shown in Fig. 11a. As expected, the uncertainty is greatest in the data with the sparsest breaking (higher b), which is already known to be biased by the pixel resolution. Within the unbiased data, the errors introduced by the short windows are small relative to the scatter of the data.

The calculation of b is also subject to uncertainty from S_{ds} . In Fig. 10, b values corresponding to four independent measurements of S_{ds} are shown. The uncertainty in the inferred S_{ds} from the radiative transfer equation is shown in Fig. 8. The SWIFT and DopBeam uncertainty is discussed in the Thomson (2012). One source of error is in the power-law fit of the structure function in Eq. (12). Lower and upper bounds of the SWIFT dissipation are propagated through the calculations using the root-mean-square error (RMSE) of the power-law fit. The resulting b error bars for SWIFT 1 are shown in Fig. 11b. These errors are comparatively small relative to the uncertainties from $\Lambda(c)$.

The sensitivity of b to choices made in the $\Lambda(c)$ processing is shown in Figs. 11c–e. For example, the threshold value used to generate the binary video frames (see the appendix) controls the number of pixels identified as

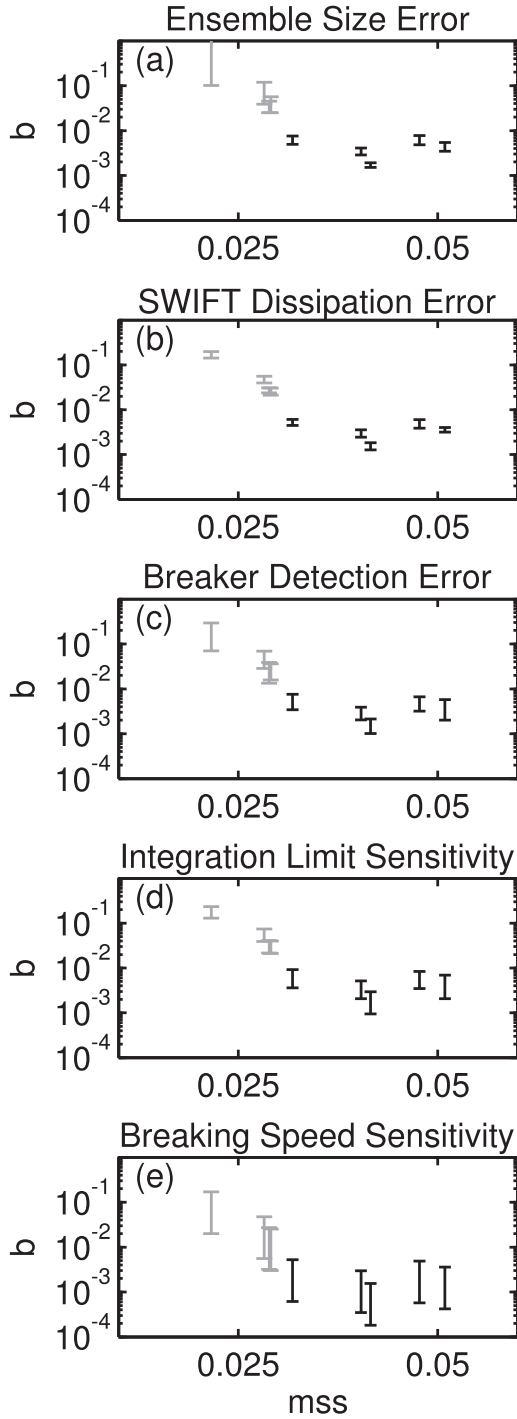


FIG. 11. Sensitivities and error bars for the b data with the SWIFT S_{ds} values. Error bars come from (a) plus or minus one std dev in the values of b from 50 runs of synthetic data, (b) estimated error in the SWIFT dissipation values, (c) varying the threshold value in converting differenced images to binary by $\pm 20\%$, (d) varying the upper limit of integration of $c^5 \Lambda(c) dc$ (originally c_p) by $\pm 20\%$, and (e) varying α in $c = \alpha c_{brk}$ by $0.7 \leq \alpha \leq 1$. Gray points indicate b values that are biased by small-scale breaking.

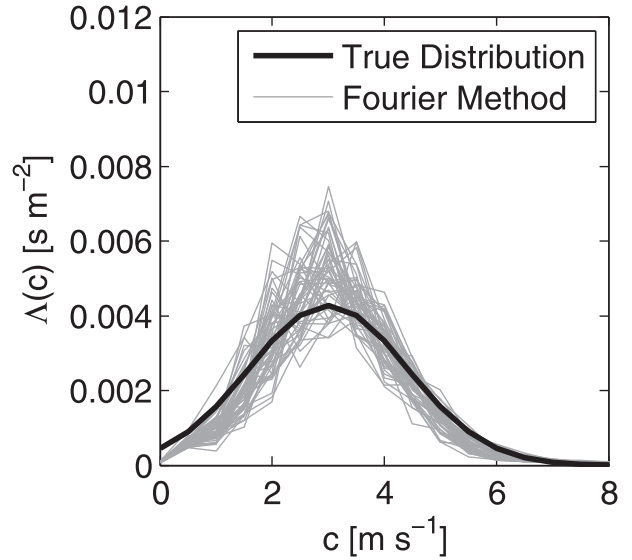


FIG. 12. Comparison of the true $\Lambda(c)$ distribution (solid black) with the estimate from the Fourier method for 50 runs of synthetic data (gray), with inputs similar to the $\Lambda(c)$ data from 21:34 UTC 14 Feb.

“breaking crests.” The effect on b of adjusting this threshold by $\pm 20\%$ is shown Fig. 11c. The error bars associated with this manipulation are roughly uniform and extend approximately half an order of magnitude. Similarly, varying the upper limit $c = c_p$ in the integration of $c^5 \Lambda(c) dc$ by $\pm 20\%$ shifts the b results by roughly a half order of magnitude, as shown in Fig. 11d.

Finally, there is some disagreement over the correct speed to assign each breaking event. In Phillips’s theory, c refers to the phase speed of the breaking wave. It has been observed, however, that the speed of the whitecap is actually somewhat less than the phase speed. Laboratory experiments (Rapp and Melville 1990; Banner and Pierson 2007; Stansell and MacFarlane 2002) show a possible linear relationship between the two speeds of the form $c_{brk} = \alpha c$, where c is the true phase speed, c_{brk} is the observed speed of the whitecap, and α ranges from 0.7 to 0.95. Moreover, Kleiss and Melville (2011) showed that the speed of advancing foam in breaking waves tends to slow over the course of a breaking event. This is consistent with the laboratory study of Babanin et al. (2010a), which showed a shortening and slowing in waves breaking from modulational instability. Because the Fourier method includes contributions from speeds throughout the duration of breaking, it distributes the contributions from a single breaking event to a number of speed bins. This interpretation of breaker speed, however, may be contrary to the original definition of the $\Lambda(c)$ function by Phillips (1985) (M. Banner 2013, personal communication). The effect on $\Lambda(c)$ of these

two modifications to the assigned breaking speed is similar—both serve to shift breaking contributions to higher phase speeds.

Using synthetic data, we have determined that the Fourier method $\Lambda(c)$ centers on the average speed of the breaking wave. Thus, for crests slowing to 55% of their maximum speed, as in Kleiss and Melville (2011), the effect is similar to using $\alpha = 0.775$. The implications of this difference are most apparent in the fifth-moment calculation, where using $\alpha = 0.7$ (the most extreme literature value) increases the magnitude of $c^5 \Lambda(c) dc$ by $\alpha^{-6} = 850\%$, as shown in Fig. 11e. Adjusting to maximum breaker speeds, our final b estimates would be $O(10^{-4})$, rather than the $O(10^{-3})$ we obtain with average breaker speeds. Thus, the slowing effect is thus similar in extreme to the bias of insufficient pixel resolution—either can increase the inferred b by over an order of magnitude.

c. Comparison with Phillips's relation

Phillips (1985) introduced the concept of a spectral “equilibrium range,” for which the nonlinear energy transfers, wind input, and dissipation are in local equilibrium. This theory explained the consistent f^{-4} shape noted by Toba (1973) and others in the tail of the frequency spectrum. The theory modified Phillips's earlier 1958 theory of a region of constant saturation, which led to an f^{-5} slope in the spectral tail. The equilibrium range has usually been assumed to begin at $k > 2k_p$, or, equivalently, $c < 0.7c_p$ (e.g., Kleiss and Melville 2010). Romero and Melville (2010) noted a transition in their wavenumber spectra from $k^{-5/2}$ (equivalent to f^{-4}) to k^{-3} (f^{-5}) at higher wavelengths and proposed that this marked a transition from equilibrium to saturation ranges. The frequency spectra in Fig. 2 appear to largely follow f^{-5} for frequencies above the peak, perhaps implying a narrow equilibrium range. This is consistent with the wave age dependency proposed in Romero and Melville (2010), as these are young, highly forced waves.

Within the equilibrium range, Phillips (1985) predicted $\Lambda(c)$ to follow the c^{-6} form of Eq. (8), based on the derived dissipation term in that region [Eq. (6)]. It has often been noted that $\Lambda(c)$ resembles c^{-6} at speeds beyond its peak (e.g., Thomson et al. 2009), as is also shown in Fig. 5. However, these speeds are not generally within the equilibrium range, as shown in Figs. 13a and 13b. In Fig. 13a, the frequency spectrum corresponding to each $\Lambda(c)$ curve is plotted as a function of phase speed using the dispersion relation. Figure 13b shows that at speeds where equilibrium may exist, $c < 0.7c_p$, $\Lambda(c)$ does not show the predicted form. Instead, a peaked curve similar to many recent studies is observed. This result implies either a flaw in Phillips's equilibrium range

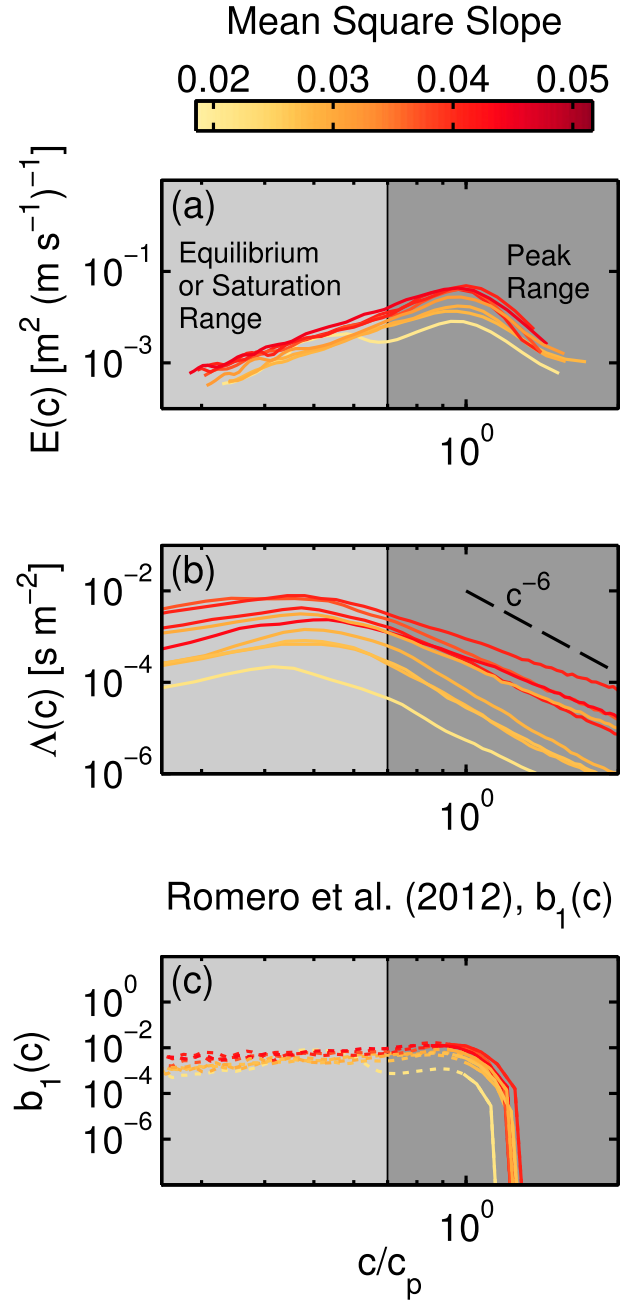


FIG. 13. (a) Wave height spectra vs normalized phase speed c/c_p . All lines colored by mss. Shading divides the spectra into the peak and equilibrium (or possibly saturation) range, using a cutoff of $0.7c_p$. (b) $\Lambda(c)$ from Fig. 5. (c) The $b_1(c)$ model from Romero et al. (2012) using the azimuthal-integrated saturation spectra, σ and coefficients $A_1 = 4.5$ and $B_T = 9.3 \times 10^{-4}$.

spectral dissipation function [Eq. (6)], significant errors in estimates of $\Lambda(c)$, or deviations from Duncan's c^5 scaling of breaking dissipation [Eq. (2)].

As described above, our wave spectra do not show a distinct equilibrium range, characterized by an f^{-4}

slope in the tail. Because Eq. (6) is only expected to hold within the equilibrium range, it could be argued that this is the source of the discrepancy in the shape of $\Lambda(c)$. The peaked $\Lambda(c)$ shape, however, has been measured in a wide variety of wave conditions. It is unlikely that this particular source of error would be universal in the literature data. Another possible issue is the lack of microbreaking measurements here and in most previous field studies. One exception is the recent study by Sutherland and Melville (2013), which used stereo IR video to improve the detection of small-scale breaking. Their $\Lambda(c)$ agree well with visible video measurements at high speeds, but extended the c^{-6} region to lower speeds. This presents the possibility that the peaked $\Lambda(c)$ within the equilibrium range noted here and throughout the literature is due to the prevalence of microbreaking in this range. More such IR measurements would be helpful for evaluating this argument.

The final potential cause of the difference between the measured $\Lambda(c)$ and Phillips's prediction is in the use of Duncan's c^5 scaling of dissipation. One way to implicitly modify Duncan's c^5 scaling is through a spectral $b(c)$ or $b(k)$. In studying wave breaking in GOTEX, Romero et al. (2012) proposed two such models of b :

$$b_1(k) = A_1(\sigma^{1/2} - B_T^{1/2})^{5/2} \quad (23)$$

and

$$b_2(k) = A_2(\tilde{\sigma}^{1/2} - \tilde{B}_T^{1/2})^{5/2}, \quad (24)$$

where σ is the azimuthal-integrated spectral saturation in wavenumber [Eq. (10)]; $\tilde{\sigma}$ is saturation normalized by the directional spreading; and A_1 , A_2 , B_T , and \tilde{B}_T are coefficients fit to their data. These models are based on the results of Banner and Pierson (2007) and Drazen et al. (2008), showing a $5/2$ power-law dependence on wave slope. In Fig. 13c, the spectral $b_1(k)$ is plotted for our data using $A_1 = 4.5$ and $B_T = 9.3 \times 10^{-4}$, which Romero et al. (2012) calculate for $\alpha = 1$ (i.e., assuming whitecap speed equals the underlying wave phase speed) and use the Janssen (1991) wind input function. The saturation spectra are calculated as in Eq. (10). The model $b(k)$ is then converted to $b(c)$ using the deep-water phase speed $c = \sqrt{g/k}$.

Two important features of the Romero et al. (2012) $b_1(c)$ are worth noting. Above c_p , $b_1(c)$ decreases dramatically due to a drop off in σ . This means that the effective exponent in the proposed c^5 Duncan scaling is actually much less than 5 in this region. This result was used to justify the upper limit of c_p in the integration of $c^5\Lambda(c)$ in the previous section. Below c_p , $b_1(c)$ is essentially flat; thus, it does not explain the discrepancy with

Eq. (8) in this region. Similarly, Romero et al. (2012) noted that their measured $b(c)$ were much higher than their model $b_1(c)$ at these low speeds. For this reason, they do not extend their calculated b to speeds less than 4.5 m s^{-1} . This region is shown with dotted lines in Fig. 13 and makes up the entire potential equilibrium range for our waves.

The $b(c)$ models from Romero et al. (2012) are based on the premise that the c^5 scaling of Duncan need only be modified to include a secondary dependence on wave slope. However, there are a number of other possible reasons for the apparent deviations from the original c^5 scaling. First, Duncan's relation was derived for steady breakers caused by a towed hydrofoil. Because ocean breaking waves are fundamentally unsteady, time derivatives may play an important role in the dissipation scaling. Although the c^5 scaling has been applied to unsteady breaking in Melville (1994) and Drazen et al. (2008) with an additional dependence on wave slope, these laboratory breakers do not necessarily simulate natural whitecaps. Ocean waves break primarily due to modulational instability, whereas laboratory waves are usually induced to break by linear superposition (Babanin 2011). In addition, three-dimensional wave effects (i.e., the short crestedness that is a signature of whitecaps) are not well simulated in flume experiments. Another characteristic of natural waves that is not included in laboratory experiments is the influence of short-wave modulation by the peak wave orbitals. Thomson and Jessup (2009) and Kleiss and Melville (2011) both corrected for this effect in their $\Lambda(c)$ calculations, but found that the change was minimal; thus, it was not performed here. However, it is still not clear what effect this modulation has on the c^5 scaling, and it has been proposed that the Duncan scaling is only applicable for the spectral peak waves where there is no modulation (Babanin 2011). This, again, is not where the Phillips (1985) equilibrium form is expected.

The original Duncan (1981) experiments need revisiting in light of these issues. The basis for scaling dissipation by c^5 comes from a momentum argument, where the change in momentum is related to the tangential component of the weight of the breaking region, per unit crest length $gA \sin\theta$. Here, θ is the wave slope and A is the cross-sectional area of the breaking region. Duncan (1981) showed experimentally that for the steady breaking waves

$$gA \sin\theta = \frac{0.015}{g \sin\theta} c^4. \quad (25)$$

Calculation of a rate of energy loss from the above force requires an additional velocity term, so it is natural to

again use c , resulting in the ultimate c^5 scaling of the dissipation rate. However, Eq. (25) has to our knowledge never been verified for unsteady ocean breaking waves. Confirmation of the original Duncan (1981) results for ocean whitecaps is a necessary, and so far missing, step to using $c^5\Lambda(c)$ to measure breaking dissipation. If the cross-sectional area of active breaking A does not scale as c^4 , the results of Duncan and Phillips cannot be applied to obtain dissipation in the field.

Additionally, the use of $c^5\Lambda(c)$ to calculate a spectral dissipation $\epsilon(c)$, as in Phillips (1985) or Romero et al. (2012), relies on the assumption of spectrally local breaking dissipation. This means that all the dissipation from a breaking wave is assigned to a single spectral component, or a small range of spectral components if a variable c is tracked throughout the breaking event. Phillips (1985) noted that this may only be applicable within the equilibrium range. It has since been shown that the breaking of the dominant waves causes dissipation of the waves at scales smaller than the peak waves (e.g., Young and Babanin 2006). Recent updates to spectral dissipation models (Ardhuin et al. 2010; Rogers et al. 2012) have used a so-called cumulative term to reproduce this effect. Thus, it is possible that some of the dissipation unaccounted for at small speeds here and in Romero et al. (2012) is in fact caused by breaking at larger scales.

d. Nonbreaking dissipation

Another consideration in dissipation estimation is the effect of nonbreaking wave dissipation, often called swell dissipation. In recent years, the observation that in waves where no breaking takes place there is still appreciable dissipation of wave energy has motivated the search for other mechanisms of wave dissipation (Babanin 2011). The most promising of these so far has been that when the wave orbital velocities achieve a certain threshold Reynolds number, the orbital motion transitions from laminar to turbulent, and this turbulence dissipates wave energy (Babanin and Haus 2009). The relevance for this study is that the total dissipation is used in calculating b , where it would be more appropriate to use only the breaking contribution to the dissipation. The magnitude of this swell dissipation is still not clear, especially in waves where breaking is also present. Babanin (2011) used laboratory measurements from Babanin and Haus (2009) and observations of swell dissipation from Ardhuin et al. (2009) to estimate the average volumetric swell dissipation as

$$\epsilon_{\text{vol}}(z) = 0.002ku_{\text{orb}}^3, \quad (26)$$

where k is the wavenumber and u_{orb} is the wave orbital velocity. Babanin and Chalikov (2012) calculated swell

dissipation in numerical simulations of a fully developed wave field and found that the volumetric dissipation scaled as

$$\epsilon_{\text{vol}}(z) = 3.87 \times 10^{-7} H_s^{1/2} g^{3/2} \exp \left[0.506 \frac{z}{H_s} + 0.0057 \left(\frac{z}{H_s} \right)^2 \right]. \quad (27)$$

Equation (26) gives dissipation rates from 1×10^{-4} to $10 \times 10^{-4} \text{ m}^2 \text{s}^{-3}$, while Eq. (27) on the order of $10^{-5} \text{ m}^2 \text{s}^{-3}$. Compared with the measured dissipation of $\epsilon_{\text{vol}} \sim 10^{-3} \text{ m}^2 \text{s}^{-3}$, these two estimates differ on whether this mechanism is an appreciable source of dissipation in this system or a very minor source. In truth, both estimates are still largely speculative, because swell dissipation has so far not been measured in the presence of breaking (Babanin and Chalikov 2012). The use of total dissipation in place of breaking dissipation in studies of $\Lambda(c)$ such as this one may lead to an overestimation of b , as breaking dissipation is less than the total dissipation. The magnitude of this bias depends on the relative importance of the breaking and swell terms.

5. Conclusions

Video and in situ measurements waves during a winter storm in the Strait of Juan de Fuca show a strong fetch dependence in wave spectral evolution and wave breaking. Heterogeneity in the wind forcing prevents drifting wave measurements from conforming to fetch-limited scaling laws, although nearby measurements at fixed stations are marginally consistent with fetch-limited scaling laws. The discrepancy is most exaggerated at short fetches where atmospheric drag is high and wave growth is rapid.

Estimates of wave breaking dissipation inferred from turbulence measurements are consistent with estimates from a wave energy budget using the RTE. There is a strong correlation between wave breaking dissipation and the mss of the waves, both of which increase along fetch.

Video-derived breaking rates and breaking crest distributions $\Lambda(c)$ also increase with mss. However, during calmer conditions, estimates of breaking rates differ between high-resolution video recorded on SWIFT drifters and low-resolution video recorded from a ship. This bias is attributed to undercounting the small breakers, and thus the $\Lambda(c)$ results during calmer conditions are not used. From the remaining $\Lambda(c)$ results, the bulk breaking parameter b is estimated to be constant through the experiment at around 10^{-3} . Error analysis indicates that

video collection and processing details, such as pixel resolution and breaker speed definition, can alter b by an order of magnitude (at least).

Compared to recent literature, these $\Lambda(c)$ results are similar in shape and magnitude. However, we suggest that many b values from recent field experiments, notably those of Thomson et al. (2009), are likely biased by subtleties of video collection and processing. We also suggest that the c^5 scaling for energy dissipation from the original Duncan (1981) laboratory experiments is of limited validity for application to whitecaps observed in the field, especially in the c^{-6} equilibrium range envisioned by Phillips (1985). This is related to recent efforts to determine a spectral $b(c)$ (e.g., Romero et al. 2012), which implicitly alter the c^5 scaling.

Acknowledgments. Thanks to the field crews from University of Washington Applied Physics Lab: Joe Talbert, Alex de Clerk, and Captain Andy Reay-Ellers. Funding provided by the National Science Foundation, the Charles V. Tom and Jean C. Gibbs Endowed Presidential Fellowship in Environmental Engineering, and the Seattle Chapter of the ARCS Foundation.

APPENDIX

Fourier Method Modifications

Modifications to the Fourier method of Thomson and Jessup (2009) are described below.

a. Calculation of incidence angle from horizon

The camera incidence angle was not constant because of the slow drift and periodic resetting of the stabilized pan and tilt. The stabilized pan and tilt adequately removed wave motions (e.g., ship roll at periods of a few seconds) from the video recordings, but contamination from lower period motions is evident in the raw video data. To remove these motions, the horizon in the undistorted image (i.e., after the lens “barrel” distortion is removed) is used as a constant reference. First, the angle above horizontal is calculated as

$$\beta = \frac{y_{\text{top}} - y_{\text{horizon}}}{y_{\text{top}} - y_{\text{bottom}}} \times 69^\circ, \quad (\text{A1})$$

where 69° is the total vertical field of view and y is in pixels. Then, the incidence angle is calculated simply as

$$\theta = 90^\circ - 69^\circ/2 + \beta. \quad (\text{A2})$$

In practice, the horizon is manually identified in four images every 30 s, and the average value of the resulting

incidence angle is used for all images in that 30 s. The incidence angle is essential for rectifying the video data to real-world coordinates (Holland et al. 1997).

b. Difference threshold

Choosing an accurate binary threshold to identify breaking crests is critical to obtaining the correct $\Lambda(c)$ distribution. Differences in lighting and foam conditions make it difficult to determine a single threshold criterion. In Thomson and Jessup (2009), a threshold based on a multiple of the image standard deviation is used, with similar results over a range of conditions. In the present study, however, the wider range of conditions necessitates a more adaptable method. Thus, the modification of a technique described in Kleiss and Melville (2011) is used, which is based on the cumulative complementary distribution of pixels:

$$W(i_t) = 1 - \int_{-\infty}^{i_t} p(i) di, \quad (\text{A3})$$

where $p(i)$ is the probability density function of the subtracted brightnesses. The main difference from Kleiss and Melville (2011) is the use of the differenced images rather than the raw frames. As shown in Fig. 3 of Kleiss and Melville (2011), $W(i_t)$ decreases from 1 to 0 as i_t increases and shows a distinct tail at high i_t , when breaking is present. This signature is also present when using differenced images. The tail is seen clearly in the second derivative L'' of the log of $W(i_t)$. As noted by Kleiss and Melville (2011), taking the threshold as the beginning of this deviation (i.e., maximum L'') produces a number of false positives in their data. To obtain better a better signal-to-noise ratio, they settle on a threshold value where L'' falls to 20% of its maximum value. The same threshold is applied here, after manually confirming that this is near the point when thresholding stops excluding more residual foam and begins cutting off the edges of true breaking crests.

c. Constant signal-to-noise filter

Thomson and Jessup (2009) describe the need to isolate the significant bands around the peak in the wavenumber-frequency spectrum when transforming to $S(c)$ to prevent noise from biasing the speed signal (Thomson and Jessup 2009, p. 1667). To this end, Thomson and Jessup (2009) restrict the integration from $S(k_y, f)$ to $S(k_y, c)$ to the points where the value of $S(k_y, f)$ is greater than 50% of the peak of $S(k_y)$. This process was slightly modified after examining the accuracy of the Fourier method with synthetic data. It was found that significant

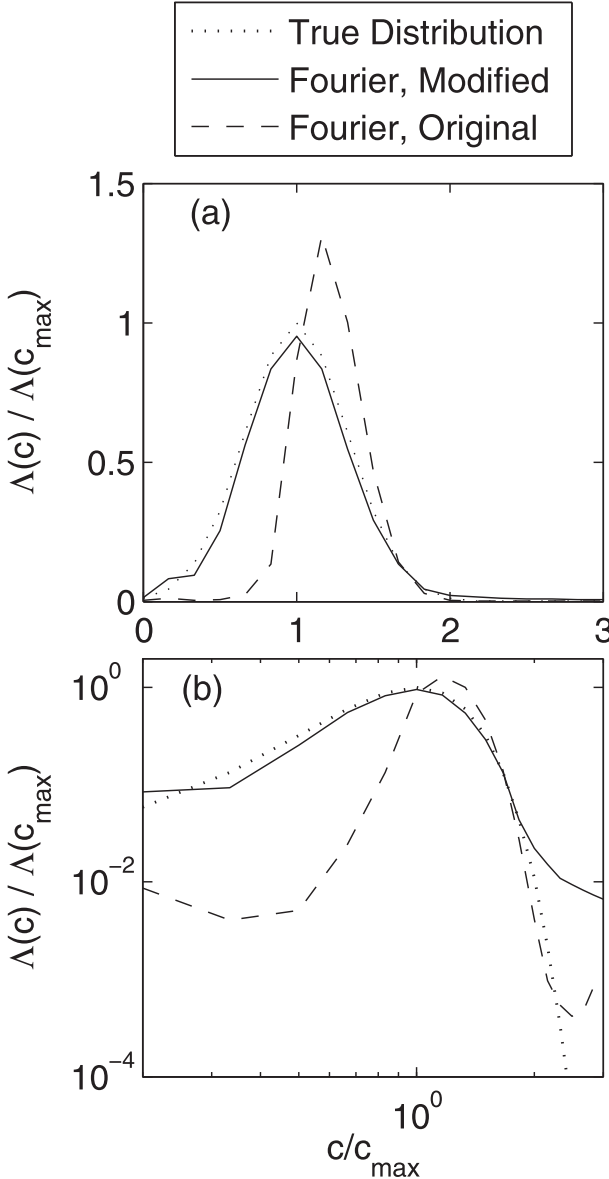


FIG. A1. Comparison of $\Lambda(c)$ results from the Fourier method with synthetic data input in (a) linear and (b) logarithmic coordinates. The true distribution (dotted) is the Gaussian input distribution for the synthetic data. Speeds and amplitudes are relative to the peak in the true distribution. The original Fourier method curve (dashed) uses the wavenumber-specific signal-to-noise filtering of Thomson and Jessup (2009). The modified Fourier method (solid) uses a constant signal-to-noise cutoff throughout the spectrum.

gains in accuracy could be made by using an integration cutoff that did not vary with the wavenumber, as shown in Fig. A1. The true $\Lambda(c)$ curve in Fig. A1 is the Gaussian function used as the input distribution to the synthetic data. The “original” $\Lambda(c)$ comes from the Fourier method as described in Thomson and Jessup (2009).

For the “modified” curve, values from wavenumbers or frequencies less than 0.2 s^{-1} (or 0.2 m^{-1}) are removed as they contain a high density of noise. Next, a constant cutoff 5% of the absolute maximum value of the remaining spectrum is used in the limits of integration around the significant band. The comparison is also shown on logarithmic axes in Fig. A1b. This plot confirms the gains in accuracy of the modified filter at both the low- and high-speed tails of the distribution, but also shows a general issue with the Fourier method at high speeds. Whereas time-domain calculations of $\Lambda(c)$ contain zeros at high speeds where no observations are measured, the Fourier method contains small, nonzero values related to the noise floor in the spectrum. These small contributions may be amplified when taking higher moments of $\Lambda(c)$. Therefore, some caution must be used in integrating $c^5 \Lambda(c)$ to large c in Eq. (5), which is discussed in section 3.

d. Width/speed bias

A central assumption in the normalization of $\Lambda(c)$ by L_{total} described above is that the width of the breaking crests is exactly one pixel, so that all $\sum I(x, y, t)$ pixels contribute to the length of the crest. However, breaking that occurs at speeds faster than one pixel per frame, $c > \Delta x / \Delta t$, will produce crests in the binary image of width:

$$n = \frac{c}{\Delta x / \Delta t}, \quad (\text{A4})$$

where Δx is the pixel width in the breaking direction, and Δt is the separation between frames (here 0.0667 s). Evidence of this effect is shown in Fig. A2a, where the average horizontal advancement of crests is plotted against their average width, weighted by crest size. These variables are well correlated, and the relation follows closely the one-to-one line predicted by Eq. (A4). To correct for the associated bias of additional pixels with faster crests, the FFT normalization of Thomson and Jessup (2009) is modified with the ratio of $\Delta x / \Delta t$ to obtain

$$\Lambda(c) = L_{\text{total}} \frac{\Delta x / \Delta t}{c} \frac{S(c)}{\int S(c) dc}. \quad (\text{A5})$$

From Eq. (4), the breaking rate can be calculated from the first moment of $\Lambda(c)$. In addition, the breaking rate can be calculated directly from the binary images as

$$R_I = \frac{\sum I(x, y, t)}{n_x n_y N \Delta t}, \quad (\text{A6})$$

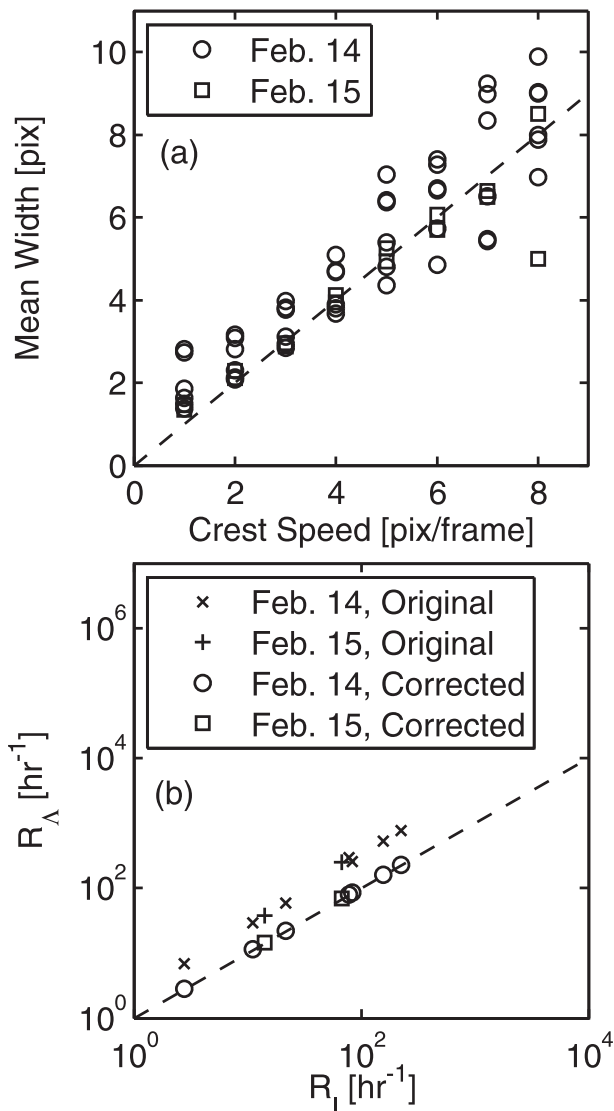


FIG. A2. (a) Comparison of mean crest width in pixels with crest advancement speed in pixels for both 14 Feb (circles) and 15 Feb (squares). (b) Comparison of calculated breaking rate from the first moment of $\Lambda(c)$, R_A , with the direct breaking rate R_I for the original distribution. The R_A are shown without width correction (original, multiplication signs for 14 Feb, plus signs for 15 Feb) and with width correction (corrected, circles for 14 Feb, squares for 15 Feb).

where n_x and n_y are the number of pixels in x and y . Carrying through the integration in Eq. (4) with the modified $\Lambda(c)$ from Eq. (A5) results in an equivalent expression as Eq. (A6). Thus, in effect the width modification amounts to rescaling $\Lambda(c)$ to match the direct breaking rate R_I . Figure A2b compares R_A from the original $\Lambda(c)$ distribution and from the width-corrected $\Lambda(c)$ with the direct breaking rate R_I . The linear trend in the original results indicates that the bias is small and

linear. The final results show identically equal values of R_I and R_A , as required by this normalization.

REFERENCES

- Agrawal, Y. C., E. A. Terray, and M. Donelan, 1992: Enhanced dissipation of kinetic energy beneath surface waves. *Nature*, **359**, 219–220.
- Anis, A., and J. N. Moum, 1995: Surface wave–turbulence interactions: Scaling $\epsilon(z)$ near the sea surface. *J. Phys. Oceanogr.*, **25**, 2025–2045.
- Ardhuin, F., B. Chapron, and F. Collard, 2009: Observation of swell dissipation across oceans. *Geophys. Res. Lett.*, **36**, L06607, doi:10.1029/2008GL037030.
- , and Coauthors, 2010: Semiempirical dissipation source functions for ocean waves. Part I: Definition, calibration, and validation. *J. Phys. Oceanogr.*, **40**, 1917–1941.
- Babanin, A. V., 2011: *Breaking and Dissipation of Ocean Surface Waves*. Cambridge University Press, 480 pp.
- , and D. Chalikov, 2012: Numerical investigation of turbulence generation in non-breaking potential waves. *J. Geophys. Res.*, **117**, C06010, doi:10.1029/2012JC007929.
- , and B. K. Haus, 2009: On the existence of water turbulence induced by non-breaking surface waves. *J. Phys. Oceanogr.*, **39**, 2675–2679.
- , D. Chalikov, I. R. Young, and I. Savelyev, 2010a: Numerical and laboratory investigation of breaking of steep two-dimensional waves in deep water. *J. Fluid Mech.*, **644**, 433–463.
- , K. N. Tsagareli, I. R. Young, and D. J. Walker, 2010b: Numerical investigation of spectral evolution of wind waves. Part II: Dissipation function and evolution tests. *J. Phys. Oceanogr.*, **40**, 667–683.
- Banner, M. L., and D. H. Peregrine, 1993: Wave breaking in deep water. *Annu. Rev. Fluid Mech.*, **25**, 373–397.
- , and W. L. Pierson, 2007: Wave breaking onset and strength for two-dimensional deep water wave groups. *J. Fluid Mech.*, **585**, 93–115.
- , A. V. Babanin, and I. Young, 2000: Breaking probability for dominant waves on the sea surface. *J. Phys. Oceanogr.*, **30**, 3145–3160.
- , J. R. Gemmrich, and D. Farmer, 2002: Multiscale measurements of ocean wave breaking probability. *J. Phys. Oceanogr.*, **32**, 3364–3375.
- CERC, 1977: Wave and water level predictions. *Shore Protection Manual*. 3rd ed. U.S. Army Coastal Engineering Research Center, 175 pp.
- Chickadel, C. C., R. A. Holman, and M. H. Freilich, 2003: An optical technique for the measurement of longshore currents. *J. Geophys. Res.*, **108**, 3364, doi:10.1029/2003JC001774.
- Ding, L., and D. Farmer, 1994: Observations of breaking wave statistics. *J. Phys. Oceanogr.*, **24**, 1368–1387.
- Dobson, F., W. Perrie, and B. Toulany, 1989: On the deep-water fetch laws for wind-generated surface gravity waves. *Atmos.–Ocean*, **27**, 210–236.
- Donelan, M., J. Hamilton, and W. H. Hui, 1985: Directional spectra of wind-generated waves. *Philos. Trans. Roy. Soc. London*, **A315**, 509–562.
- , M. Skafel, H. Gruber, P. Liu, D. Schwab, and S. Venkatesh, 1992: On the growth rate of wind-generated waves. *Atmos.–Ocean*, **30**, 457–478.
- Drazen, D., W. K. Melville, and L. Lenain, 2008: Inertial scaling of dissipation in unsteady breaking waves. *J. Fluid Mech.*, **611**, 307–332.

- Duncan, J. H., 1981: An experimental investigation of breaking waves produced by a towed hydrofoil. *Proc. Roy. Soc. London, A*, **377**, 331–348.
- , 1983: The breaking and non-breaking wave resistance of a two-dimensional hydrofoil. *J. Fluid Mech.*, **126**, 507–520.
- , 2001: Spilling breakers. *Annu. Rev. Fluid Mech.*, **33**, 519–547.
- Gemmrich, J. R., 2010: Strong turbulence in the wave crest region. *J. Phys. Oceanogr.*, **40**, 583–595.
- , and D. Farmer, 1999: Observations of the scale and occurrence of breaking surface waves. *J. Phys. Oceanogr.*, **29**, 2595–2606.
- , and —, 2004: Near-surface turbulence in the presence of breaking waves. *J. Phys. Oceanogr.*, **34**, 1067–1086.
- , T. Mudge, and V. Polonichko, 1994: On the energy input from wind to surface waves. *J. Phys. Oceanogr.*, **24**, 2413–2417.
- , M. L. Banner, and C. Garrett, 2008: Spectrally resolved energy dissipation rate and momentum flux of breaking waves. *J. Phys. Oceanogr.*, **38**, 1296–1312.
- Hasselmann, K., and Coauthors, 1973: Measurements of wind-wave growth and swell decay during the Joint North Sea Wave Project (JONSWAP). *Dtsch. Hydrogr. Z.*, **8** (12), 1–95.
- Herbers, T. H. C., P. F. Jessen, T. T. Janssen, D. B. Colbert, and J. H. MacMahan, 2012: Observing ocean surface waves with GPS-tracked buoys. *J. Atmos. Oceanic Technol.*, **29**, 944–959.
- Holland, K. T., R. A. Holman, T. C. Lippmann, J. Stanley, and N. Plant, 1997: Practical use of video imagery in nearshore oceanographic field studies. *IEEE J. Oceanic Eng.*, **22**, 81–92.
- Janssen, P. A. E. M., 1991: Quasi-linear theory of wave generation applied to wave forecasting. *J. Phys. Oceanogr.*, **21**, 1631–1642.
- Jessup, A., and K. Phadnis, 2005: Measurement of the geometric and kinematic properties of microscale breaking waves from infrared imagery using a PIV algorithm. *Meas. Sci. Technol.*, **16**, 1961–1969.
- , C. Zappa, and M. Loewen, 1997: Infrared remote sensing of breaking waves. *Nature*, **385**, 52–55.
- Kitaigorodskii, S., 1962: Contribution to an analysis of the spectra of wind-caused wave action. *Izv. Akad. Nauk SSSR Geophys.*, **9**, 1221–1228.
- , M. Donelan, J. L. Lumley, and E. A. Terray, 1983: Wave-turbulence interactions in the upper ocean. Part II: Statistical characteristics of wave and turbulent components of the random velocity field in the marine surface layer. *J. Phys. Oceanogr.*, **13**, 1988–1999.
- Kleiss, J. M., and W. K. Melville, 2010: Observations of wave breaking kinematics in fetch-limited seas. *J. Phys. Oceanogr.*, **40**, 2575–2604.
- , and —, 2011: The analysis of sea surface imagery for whitecap kinematics. *J. Atmos. Oceanic Technol.*, **28**, 219–243.
- Large, W., and S. Pond, 1981: Open ocean momentum flux measurements in moderate to strong winds. *J. Phys. Oceanogr.*, **11**, 324–336.
- Loewen, M. R., and W. K. Melville, 1991: Microwave backscatter and acoustic radiation from breaking waves. *J. Fluid Mech.*, **224**, 601–623.
- Melville, W. K., 1994: Energy dissipation by breaking waves. *J. Phys. Oceanogr.*, **24**, 2041–2049.
- , 1996: The role of surface-wave breaking in air-sea interaction. *Annu. Rev. Fluid Mech.*, **28**, 279–321.
- , and P. Matusov, 2002: Distribution of breaking waves at the ocean surface. *Nature*, **417**, 58–63.
- Phillips, O. M., 1958: The equilibrium range in the spectrum of wind-generated ocean waves. *J. Fluid Mech.*, **4**, 426–434.
- , 1985: Spectral and statistical properties of the equilibrium range in wind-generated gravity waves. *J. Fluid Mech.*, **156**, 495–531.
- , F. Posner, and J. Hansen, 2001: High range resolution radar measurements of the speed distribution of breaking events in wind-generated ocean waves: Surface impulse and wave energy dissipation rates. *J. Phys. Oceanogr.*, **31**, 450–460.
- Plant, W. J., 2012: Whitecaps in deep water. *Geophys. Res. Lett.*, **39**, L16601, doi:10.1029/2012GL052732.
- Rapp, R. J., and W. K. Melville, 1990: Laboratory measurements of deep-water breaking waves. *Philos. Trans. Roy. Soc. London, A*, **331**, 735–800.
- Rogers, W. E., A. V. Babanin, and D. W. Wang, 2012: Observation-consistent input and whitecapping dissipation in a model for wind-generated surface waves: Description and simple calculations. *J. Atmos. Oceanic Technol.*, **29**, 1329–1346.
- Romero, L., and W. K. Melville, 2010: Airborne observations of fetch-limited waves in the Gulf of Tehuantepec. *J. Phys. Oceanogr.*, **40**, 441–465.
- , —, and J. M. Kleiss, 2012: Spectral energy dissipation due to surface wave breaking. *J. Phys. Oceanogr.*, **42**, 1421–1444.
- Smith, P. C., and J. I. Macpherson, 1987: Cross-shore variations of near-surface wind velocity and atmospheric turbulence at the land-sea boundary during CASP. *Atmos.–Ocean*, **25**, 279–303.
- Stansell, P., and C. MacFarlane, 2002: Experimental investigation of wave breaking criteria based on wave phase speeds. *J. Phys. Oceanogr.*, **32**, 1269–1283.
- Sutherland, P., and W. K. Melville, 2013: Field measurements and scaling of ocean surface wave-breaking statistics. *Geophys. Res. Lett.*, **40**, 3074–3079, doi:10.1029/2012GL050584.
- Terray, E., M. Donelan, Y. Agrawal, W. Drennan, K. Kahma, A. Williams, P. Hwang, and S. Kitaigorodskii, 1996: Estimates of kinetic energy dissipation under breaking waves. *J. Phys. Oceanogr.*, **26**, 792–807.
- Thomson, J., 2012: Wave breaking dissipation observed with “swift” drifters. *J. Atmos. Oceanic Technol.*, **29**, 1866–1882.
- , and A. Jessup, 2009: A Fourier-based method for the distribution of breaking crests from video observations. *J. Atmos. Oceanic Technol.*, **26**, 1663–1671.
- , —, and J. Gemmrich, 2009: Energy dissipation and the spectral distribution of whitecaps. *Geophys. Res. Lett.*, **36**, L11601, doi:10.1029/2009GL038201.
- Thorpe, S., 1995: Dynamical processes of transfer at the sea surface. *Prog. Oceanogr.*, **35**, 315–352.
- Toba, Y., 1973: Local balance in the air-sea boundary process. *J. Oceanogr. Soc. Japan*, **29**, 209–220.
- Wiles, P., T. P. Rippeth, J. Simpson, and P. Hendricks, 2006: A novel technique for measuring the rate of turbulent dissipation in the marine environment. *Geophys. Res. Lett.*, **33**, L21608, doi:10.1029/2006GL027050.
- Yelland, M., P. Taylor, I. Consterdine, and M. Smith, 1994: The use of the inertial dissipation technique for shipboard wind stress determination. *J. Atmos. Oceanic Technol.*, **11**, 1093–1108.
- Young, I. R., 1999: *Wind Generated Ocean Waves*. Elsevier Ocean Engineering Book Series, Vol. 2, Elsevier, 287 pp.
- , and A. V. Babanin, 2006: Spectral distribution of energy dissipation of wind-generated waves due to dominant wave breaking. *J. Phys. Oceanogr.*, **36**, 376–394.